Master's Thesis

Synthesis of High-energy-density
Li- and Mn-rich Cathode Materials
via Morphology Control and Surface Modification

Hyejin Park

School of Energy and Chemical Engineering

(Energy Engineering(Battery Science and Engineering))

Ulsan National Institute of Science and Technology

2023

Synthesis of High-energy-density
Li- and Mn-rich Cathode Materials
via Morphology Control and Surface Modification

Hyejin Park

School of Energy and Chemical Engineering

(Energy Engineering(Battery Science and Engineering))

Ulsan National Institute of Science and Technology

Synthesis of High-energy-density
Li- and Mn-rich Cathode Materials
via Morphology Control and Surface Modification

A thesis/dissertation submitted to
Ulsan National Institute of Science and Technology
in partial fulfillment of the
requirements for the degree of
Master of Science

Hyejin Park

12.06.2022 of submission
Approved by
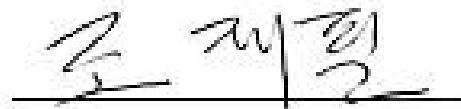
_____
Advisor
Jaephil Cho

Synthesis of High-energy-density
Li- and Mn-rich Cathode Materials
via Morphology Control and Surface Modification

Hyejin Park

This certifies that the thesis/dissertation of Hyejin Park is approved.

12.06.2022 of submission

Signature
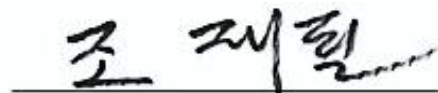
Advisor: Jaephil Cho

Signature

Youngsik Kim

Signature
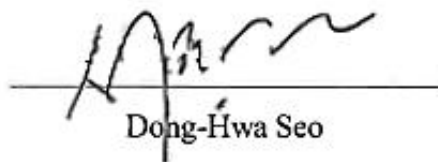
Dong-Hwa Seo

Abstract

Li- and Mn- rich cathodes (LMRs) are considered as next-generation cathode materials with their high theoretical specific capacity to realize high-energy-density Li-ion batteries. However, LMRs have difficulty in practical applications due to their intrinsic problems. Generally synthesized LMRs with small particle size have trouble achieving high volumetric energy density. Also, the presence of Li_2MnO_3 phase which requires chemical activation process at a high-voltage range triggers chemical irreversibility, resulting in low initial Coulombic efficiency (I.C.E), severe voltage decay and low rate capability. In order to solve these problems, a simultaneous modification is introduced to the particles: morphology control and surface coating. Flake-type morphology with increased primary particle size not only enables to achieve high electrode density nearly up to $3.0 gcc^{-1}$, but also reduces the contact area with electrolyte to enhance the cycle stability. The flake-type LMRs exhibit a good capacity retention of 95.9% and a low voltage decay of 0.045V after 40 cycles. High irreversibility caused by large particle size is improved by the surface coating with AlF_3. The Li_2MnO_3 phase can be activated rapidly in the first cycle with the AlF_3 coating layer, which makes the initial reversible specific capacity much higher. As a result, AlF_3-coated LMRs with flake-type shape show high I.C.E of 84.6% with a superior discharge capacity of 265mAh/g. Moreover, it is demonstrated that the AlF_3 coating layer prevents the severe phase transition to the rock salt phase by mitigating the extraction of excess lithium ions and oxygen gas at the interface. This work suggests that AlF_3 surface coating on flake-type shaped particles is an effective strategy for achieving both the high volumetric energy density and high performance LMR cathode materials.

Contents

Abstract

List of Figures

List of Tables

List of Figures

List of Tables

I. Introduction

    Lithium ion batteries (LIBs) have been widely used in customer electronics and devices for the past few years. Recently, with the advent of electronic vehicles (EVs) and energy storage systems (ESSs), the most influential factors in the LIB market have been turning into these large-scale energy storage system (**Figure 1**).[3, 16] As environmental regulations for carbon neutrality are getting stricter to prevent climate change and depletion of fossil fuels around the world, the use of internal combustion engines is decreasing. Instead, the use of EVs, also called eco-friendly cars, is increasing. Likewise, the operation of ESS, which is essential for the storage of renewable energy is also gradually increasing. LIBs show higher performance in terms of energy density, power density, and cycle life than any other battery systems (lead-acid and nickel metal hybrid), thus, LIBs have been introduced into EVs and ESSs widely.[17, 18] However, EVs have a disadvantage in that the driving distance, which is directly proportional to the battery capacity, is not long enough to compare with the existing internal combustion engine vehicles.[19] Among the four main elements of LIBs; a cathode, an anode, an electrolyte, and a separator, a cathode has the greatest influence on determining the capacity of a battery because it shows smaller capacity than the anode material. Therefore, the development of a cathode material with the high-energy-density is necessary to improve the performance of LIBs.
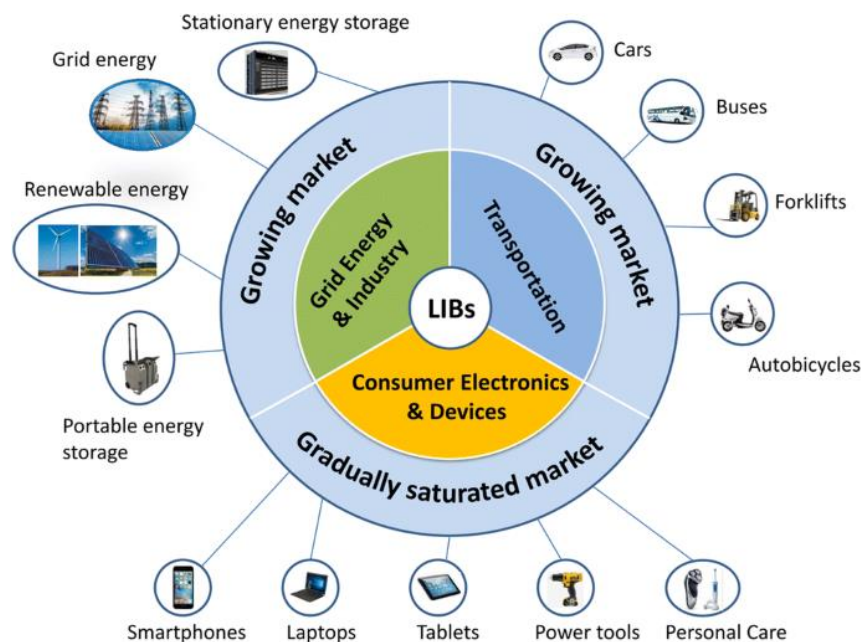
Figure 1. Applications of LIBs in the three main fields including consumer electronics and devices, transportation, as well as grid energy and industry.[3]

1.1 Co-free Li-, Mn- rich oxide (LMR) as a promising cathode materials

Li-, Mn-rich cathode (LMR), also called over-lithiated oxide (OLO), has been in the spotlight for a long time as a promising cathode material due to its high theoretical capacity exceeding 250mAh/g. This is because they have excess lithium ions available during electrochemical reactions. With this high specific capacity, it is possible to increase the energy density by 50% or more compared to commercial cathode materials, such as $LiCoO_2$ (LCO) and Li [Ni, Co, Mn/Al] O_2 (NCM/NCA) (**Figure 2**).[9, 20] LMRs have a layered structure in which rhombohedral $LiMO_2$ (M=transition metal) compounds with R-3m structure and monoclinic Li_2MnO_3 compounds with C2/m structure coexist, as shown in **Figure 3**.[5, 12, 21] Since lithium ions are present in the transition metal layers as well as in the lithium layers, more lithium ions can be utilized. With this unique structure, high capacity is achieved. Furthermore, the presence of Li_2MnO_3 phase and its activation process make more active sites for redox reactions. As shown in **Figure 4**, the extraction of lithium and oxygen ions arises from the Li_2MnO_3 phase during the first charge, leading to the voltage plateau above 4.4V. When Li_2O is completely extracted from the electrochemically inactive Li_2MnO_3 structure during initial charge processes, electrochemically active MnO_2 is formed. This process is called chemical activation of LMRs. After the Li_2MnO_3 phase is activated, lithium ions are able to intercalate into MnO_2 structure to be $LiMnO_2$ accompanying the reduction of manganese.[7]
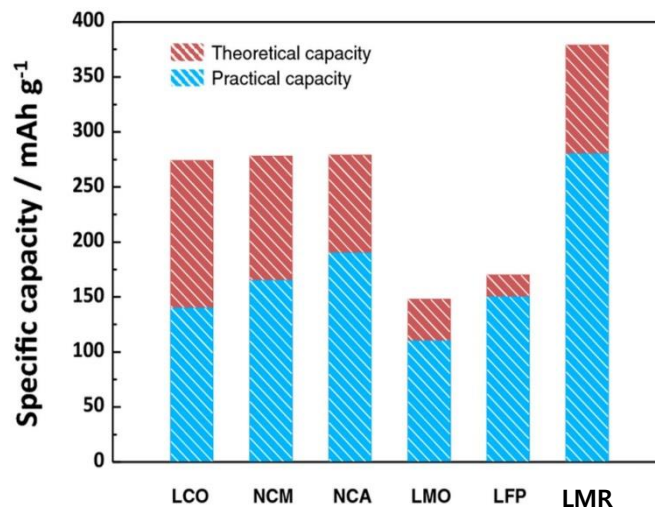
Figure 2. Comparison of theoretical and practical specific gravimetric capacities of representative cathode materials (Theoretical value is calculated based on the total amount of Li ions in the formula units).[9]
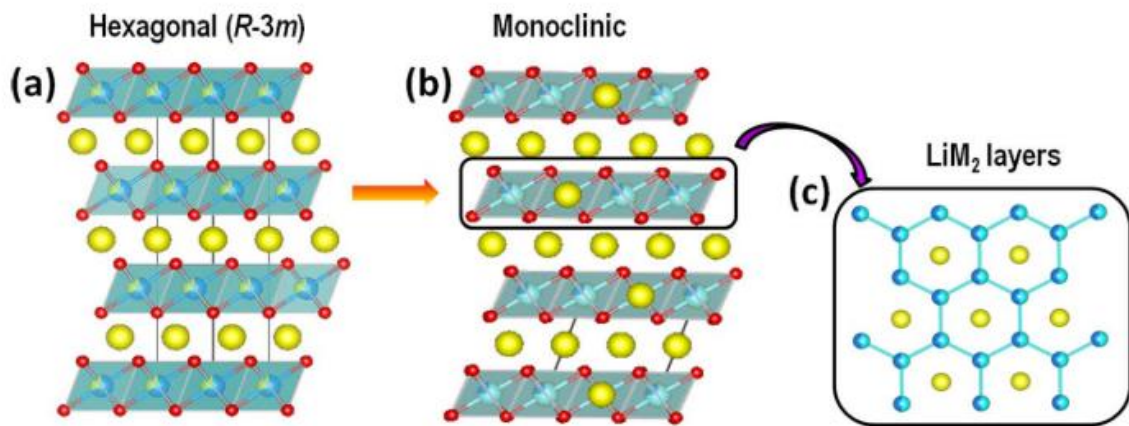
Figure 3. Structural representation of (a) O3-type layered oxides (b) the overall cell of Li-rich layered oxides described as monoclinic and (c) M / Li ordering within LiM2 layer leading to a honeycomb pattern.[5]
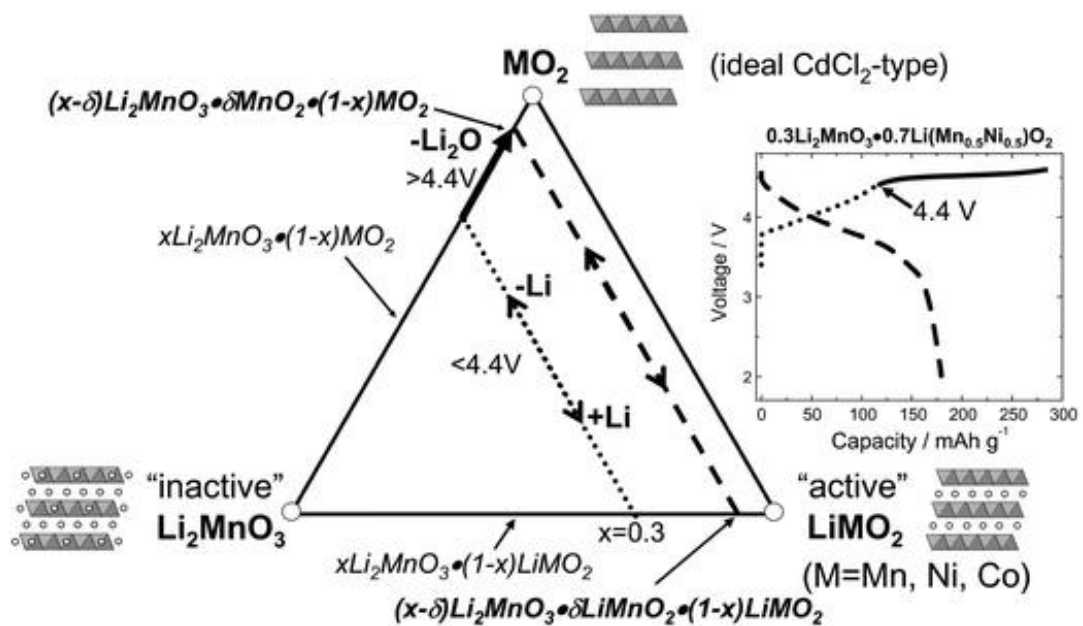
Figure 4. Compositional phase diagram showing the electrochemical reaction pathways for a $x\text{Li}_2\text{MnO}_3 \cdot (1 - x)\text{LiMO}_2$ electrode.[7]

1.2 Intrinsic problems of LMRs

The presence of Li_2MnO_3 phase induces the poor kinetics of LMRs. LMRs need to be chemically activated at a high voltage range due to the presence of Li_2MnO_3 phase. It acts as a "double-edged sword", which greatly contributes to high capacity but leads to severe intrinsic problems simultaneously. As shown in **Figure 6**, the electrochemical reaction of the first charge process can be divided into two. During the first reaction, which is characterized by the voltage profile showing S-shape curve, $LiMO_2$ (M= Mn, Ni) phase is charged. It means that the oxidation of transition metal in the $LiMO_2$ phase happens between 3.8V and 4.4V. The voltage plateau that appears above 4.4V indicates the second reaction, where the charge of Li_2MnO_3 phase happens. The valence state of manganese in Li_2MnO_3 is Mn^{4+}, and it is reduced to Mn^{3+} at this flat voltage region. During this process, lithium ions and oxygen are extracted, resulting in the formation of MnO_2 phase. It implies that the Li_2MnO_3 phase can be chemically activated into $LiMnO_2$ or $LiMn_3O_4$ phase during the subsequent discharge process.[7, 22-24] However, it also means that the lithium ions extracted from the transition metal layers cannot re-intercalate into the former place. This limited degree of lithium acceptance leads to the increased irreversible capacity and low I.C.E.[12]
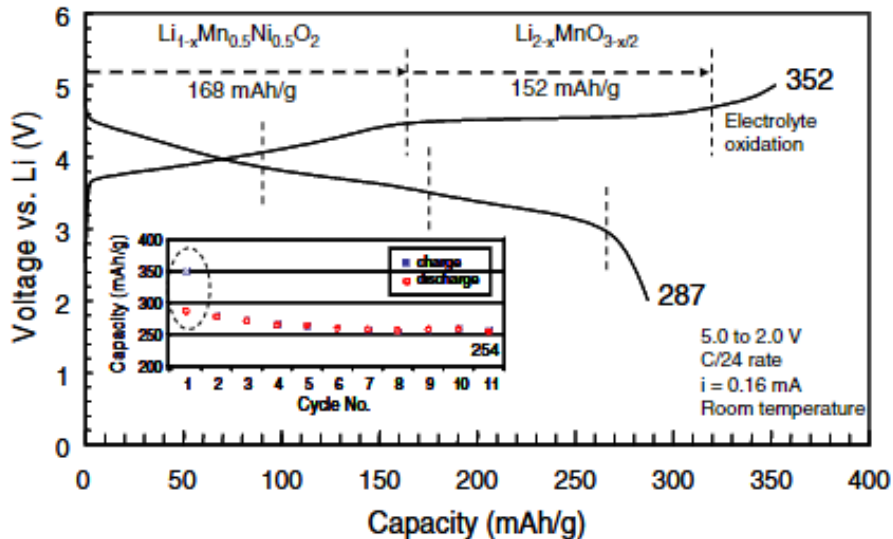
Figure 6. Initial charge/discharge profiles of a Li / $0.3Li_2MnO_3 \cdot 0.7LiMn_{0.5}Ni_{0.5}O_2$ cell (5.0–2.0 V).[7]

Another problem that the presence of Li_2MnO_3 phase causes is the excessive extraction of oxygen gas from the surface. The Li_2MnO_3 phase enables to achieve high theoretical capacity with the unique structure. In fact, the theoretical capacity is higher than the calculated capacity of the cationic redox reaction. It suggests that the reason why it is possible for LMRs to show high specific capacity is not just an excessive amount of lithium ions. Researches about this phenomenon has been actively conducted, and some researchers have suggested the contribution of oxygen ions. In other words, oxygen ions in the transition metal oxides can take part in electrochemical reactions. Other conventional cathode materials which have a layered structure use transition metal only as the source of electrochemical reactions. Unlike them, LMRs can bring about the oxygen redox reactions due to their own unique structures. For conventional cathode materials, LCO and NCM/NCA with a single layered structure, the local environment around the oxygen is only Li-O-M (M=transition metal). On the other hand, since LMR has Li_2MnO_3 structure as well as $LiMO_2$, lithium ions are also present in transition metal layers. As a result, two types of local environments of oxygen exist, Li-O-M and Li-O-Li. In general, the relative energy level is strongly dependent on the chemical bonding of the compound, and it determines where the electrochemical reaction occurs. That is to say, in the case of the cathode materials with a layered oxide structure, the relative energy level of the transition metal versus oxygen is very important to know where the oxidation reaction occurs. During the oxidation reaction, electrons are extracted from the highest occupied molecular orbital (HOMO) level.[25] When LMRs are delithiated during the first charge process, HOMO level is the e_g orbital of the transition metal-dominant states. It indicates the cationic redox reaction happens. As the degree of delithiation increases, however, the energy level of oxygen increases and strong overlap between metal d-band and oxygen p-band is triggered. As a result, oxidation happens in the oxygen-dominant states, leading to anionic redox reaction.[1, 26, 27] It is well illustrated in **Figure 7.** After the first cycle with high operating voltage range, the oxygen vacancies or partially oxidized oxygen anions are formed through the redox reaction of oxygen ions in the unique structure with Li_2MnO_3 phase. These electrochemically active oxygen states are used as the sources for the extra capacity of LMRs.[28] However, the irreversible capacity loss is triggered at the same time as the electrochemically active oxygen recombines into O_2 gas.
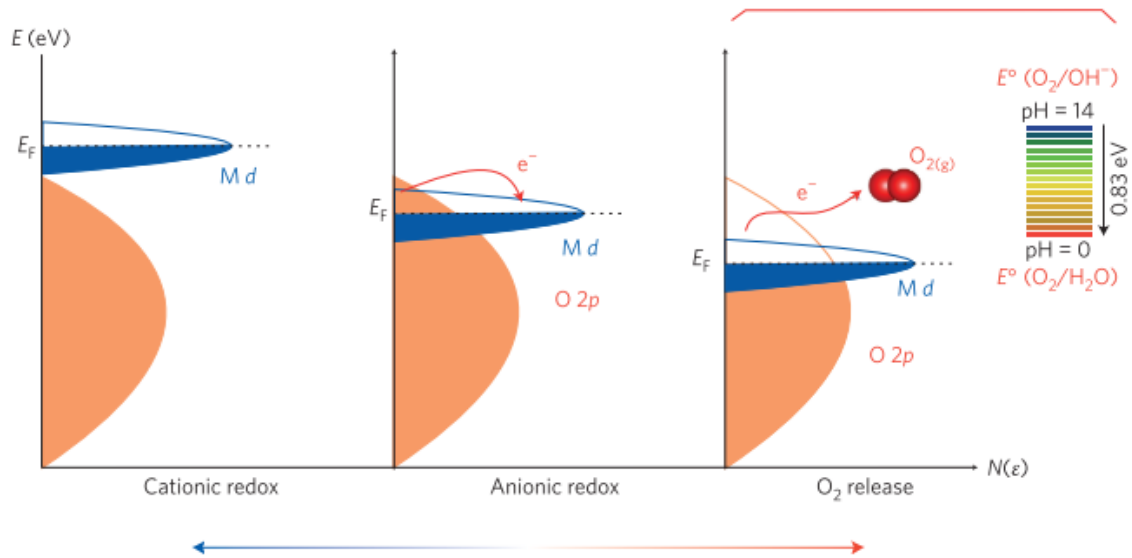
Figure 7. Schematic representation of the energy level versus density of states N(ε), showing the respective motion of the metal d band with respect to the oxygen p band in going from cationic to anionic redox processes and then O$_2$ release.[1]

The layered-to-spinel phase transition, which is a well-known structural change of LMRs, is also closely related to the activation of Li$_2$MnO$_3$ phase. **Figure 8** shows a schematic illustration of this phase transition mechanism in detail. As mentioned above, LMRs have a layered structure in which LiMO$_2$ with rhombohedral phase and Li$_2$MnO$_3$ with monoclinic phase coexist. During the initial few cycles, the chemical activation of Li$_2$MnO$_3$ phase happens gradually. The degree of activation is greatest in the first cycle. In other words, lithium ions present in both Li layers and transition metal layers are released during the first charge process most actively. Oxygen gas evolution occurs at the same time. As a result, transition metals migrate into the Li layer without the isolation of the oxygen layer, generating Li-poor cubic spinel structure. High irreversible capacity for the first cycle is accompanied by this phase transition.[13, 29] It results in low initial Coulombic efficiency (I.C.E) compared to other cathode materials.
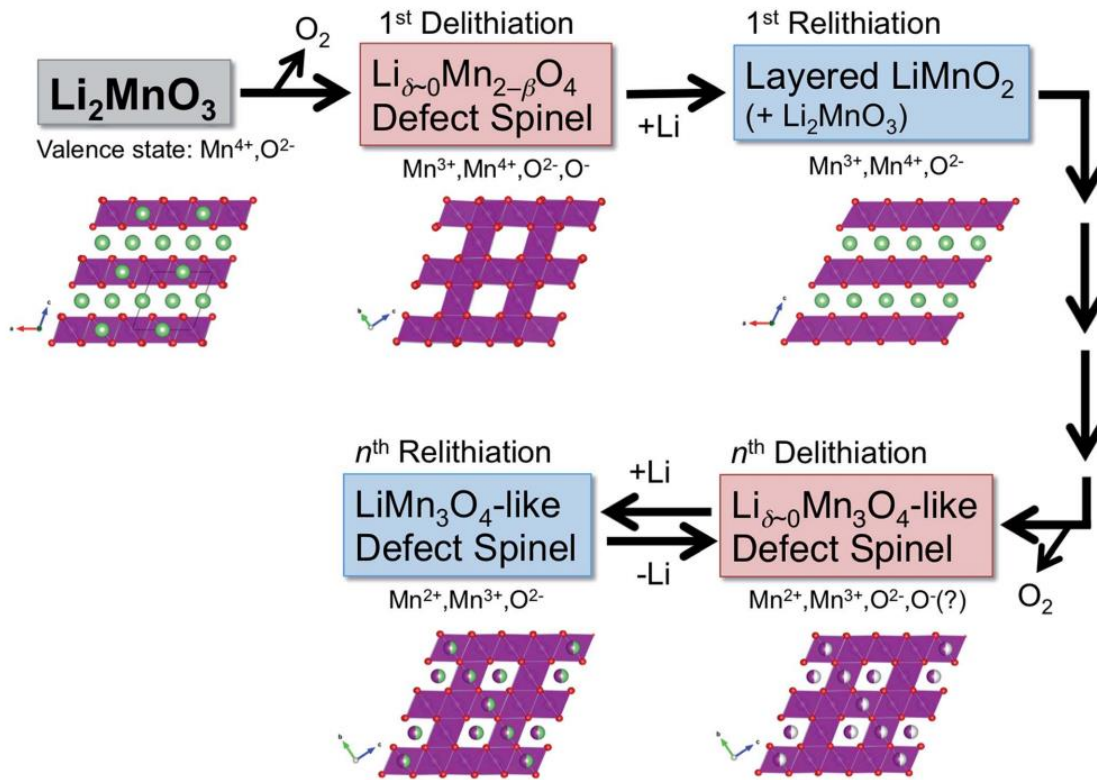
Figure 8. Schematic illustration of the layered-to-spinel phase transformation in Li_2MnO_3 during the initial cycle and after the multiple cycles.[13]

When the lithium ions are re-inserted into the cathode after the first charge, most of the lithium ions are intercalated into the Li layer. Then, the structure is consisted of a number of layered $LiMO_2$-like phase and a little of Li_2MnO_3 phase, which is not fully activated in the first delithiation process. During the following few cycles, the rest of Li_2MnO_3 phase is gradually activated, and the valence state of Mn is decreased from 4+ to 3+. Even after the activation is completed, the oxidation number of Mn ion decreases with repeated cycles. This is because oxygen ions are continuously oxidized and released as O_2 gas from the surface of LMRs. It causes Mn ions to be reduced for charge compensation. Consequently, a defect spinel structure is formed from a certain moment, whether lithium ions are intercalated or deintercalated.[13]

However, this is not the end of the phase transformation. Depending on the degree of oxygen deficiency, a more severe phase transition to the rock-salt phase can occur. In order to utilize the excess lithium ion sources of Li_2MnO_3 phase completely, charging at a high voltage range over 4.4V is required. The problem is that it has fatal influences on the phase transition and causes the degradation of electrochemical performances. The activation process is accompanied by irreversible oxygen and lithium ion extraction. As the LMRs have higher crystallinity with more Li_2MnO_3 contents, it becomes more difficult to activate the Li_2MnO_3 phase. Then, the irreversibility would be increasing and the cycling performance would be deteriorated. Furthermore, surface oxygen release during the activation process induces a structural evolution. As the degree of oxygen oxidation increases, the transition metal irreversibly migrates to the Li layer. It forms a disordered rock-salt structure which has an oxygen-deficient phase. **Figure 9** explains the process of structural change of LMRs from the layered to the rock-salt phase, and **Figure 10** shows the HR-STEM images on the surface of LMRs comparing before and after cycling. A large structural change occurs due to the migration of transition metal and the emission of oxygen gas at the surface. As a result, LMRs have a disordered rock-salt structure where the transition metal occupies the Li layer. Since it prevents the diffusion of lithium ions, structural instability and voltage decay are increased, leading to high overpotential.[2, 6, 30]
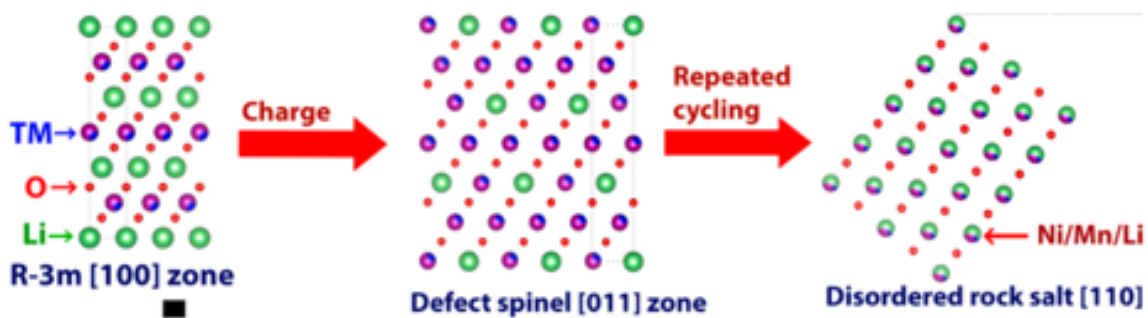
Figure 9. Atomic models explaining the structural evolution pathway based on the close observation from the structural changes in cycled materials.[6]
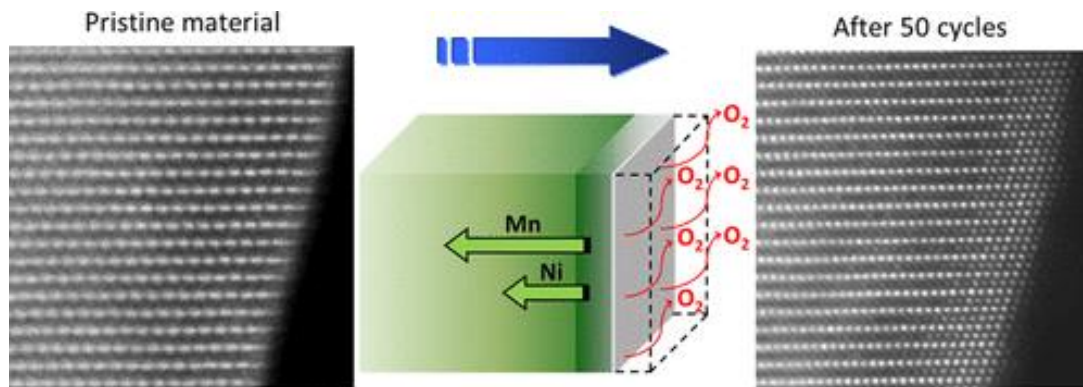
Figure 10. Mechanistic diagram of Mn and Ni ion migration differences upon cycling and its relation to phase transformation.[2]

As shown in **Figure 11a**, when comparing the discharge voltage profile of the 1st and 2nd cycle with that of the 25th cycle, the severe voltage decay occurs with a large change in voltage profile itself. A change in voltage profile is usually originated from the lattice structural transformation. Thus, it can be predicted that a large phase transition happens during the first cycle owing to the activation of Li_2MnO_3 phase. Then, a structural change has kept happening until the 25th cycle. On the other hand, the shape of voltage profile remains relatively similar after the 25th cycle, even though the capacity is greatly decreased due to the voltage drop. It demonstrates that the phase transition has finished to some extent, and voltage decay and capacity drop are mainly caused by the high overpotential caused by the poor kinetics of the finally generated structure.[14]

The dQ/dV plots in **Figure 11b** can confirm the previous results. As for the charge process, the peak intensity around 3.8V is dominant in the first cycle. It indicates that the oxidation of transition metal happens within the layered structure. Above 4.4V, the peak that indicates the oxidation of Li_2MnO_3 phase can be also observed. From the second cycle, however, the dominant peak is shifted to 3.3V and the peak around 4.4V is disappeared. It indicates that the Li_2MnO_3 phase is activated during the first charge process. The important thing to note is the change in the peak position during the discharge process. The peak around 3.3V is attributed to the reduction of $Mn^{4+/3+}$ in the layered structure. As spinel-like phase is generated to some extent, the peak position is shifted into 3.0V. When the phase transition to the spinel structure happens to a great degree, the dominant peak is located in 2.8V.[31] According to the fact that the degree of voltage difference is the highest between the 1st and 25th cycle, structural transformation to spinel phase occurs largely in this period. With this result, it can be inferred that the increase of spinel phase with the activation of Li_2MnO_3 phase is the origin of voltage decay during the initial cycles.
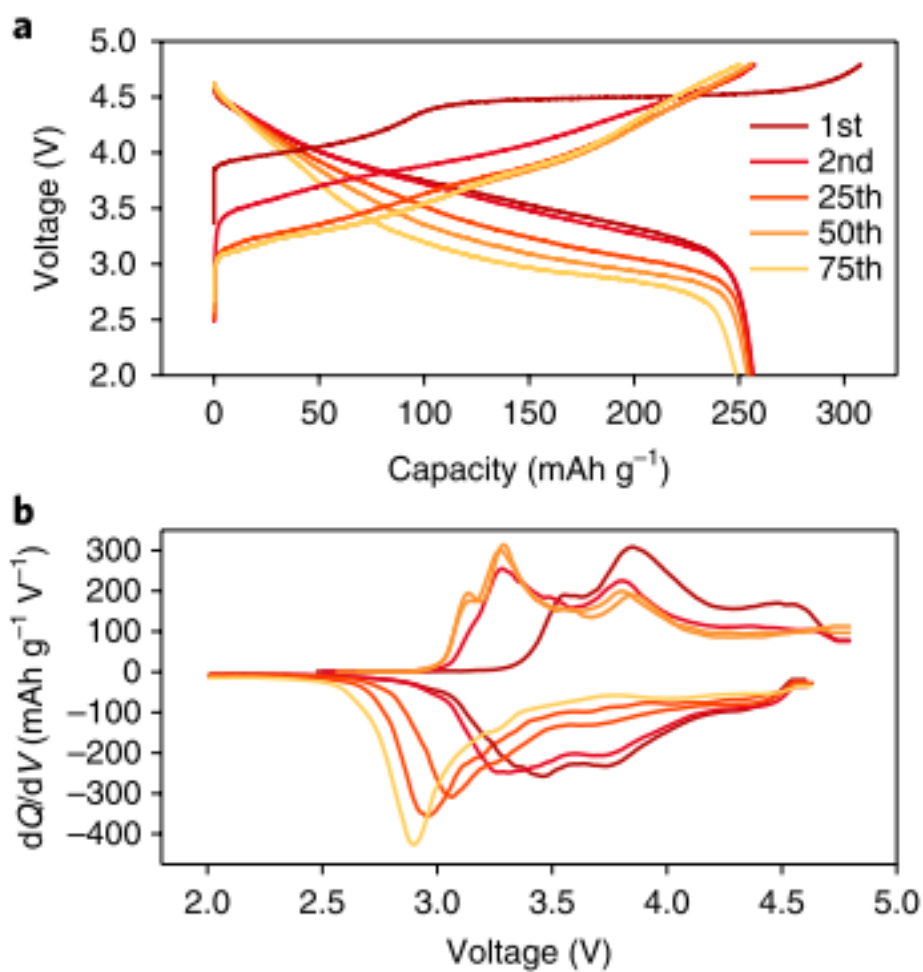
Figure 11. Electrochemical characterization of $Li_{1.2}Ni_{0.15}Co_{0.1}Mn_{0.55}O_2$. (a) Charge–discharge curves for $Li_{1.2}Ni_{0.15}Co_{0.1}Mn_{0.55}O_2$ for the 1st, 2nd, 25th, 50th and 75th cycles. (b) dQ/dV plot of $Li_{1.2}Ni_{0.15}Co_{0.1}Mn_{0.55}O_2$ for the 1st, 2nd, 25th, 50th and 75th cycles.[14]

1.3 Fundamental challenges of LMRs in practical perspectives

1.3.1 Low electrode density with small-sized primary particles

In addition to the fundamental problems arising from their unique structure, LMRs also have several challenging issues that prevent their commercialization in a practical view. In order to make their practical application feasible, their problems should be resolved. First of all, it is required to develop a cathode material capable of not only showing high specific capacity but also high electrode density to realize high-energy-density batteries. LMRs can realize high specific capacity, but they have difficulty in achieving high electrode density due to their small primary particle size and porous structure. That is why generally synthesized LMRs have low volumetric energy density. **Figure 12a and 12b** show the electrochemical performances of LMRs with the low electrode density (Low ED) and the high electrode density (High ED). These results indicate that the conventional LMRs with small primary particle size has hindered achieving high electrode density. The voltage profile and discharge capacity during the formation cycle are similar each other, regardless of electrode density. On the other hand, the cycle retention is greatly reduced as the electrode density increases. Also, as shown in **Figure 12c and 12d**, the thicker SEI layer is generated on the counterpart anodes of LMRs with High ED.[5] Because the small particle size and porous structure lead to the large surface area, it causes more side reactions with liquid electrolyte. As the oxygen evolution accompanying phase transition happens at the interface, the reactive oxygen species generated promote severe side reactions, resulting in fast capacity fade. Consequently, LMRs show the significant voltage decay and low capacity retention during the cycles. Enhancing the electrode density may generate the cracks inside the secondary particles, and accelerate the degradation mechanism. As a result, cycling stability is severely deteriorated.

Increasing the size of the primary particles seems to be able to solve this problem simply, but it triggers more critical issues. Since it becomes more difficult to activate the Li_2MnO_3 phase completely at the first cycle, irreversible capacity is increased and energy density is severely lowered. In order to achieve the full activation of Li_2MnO_3 phase, a charge process at a high operating voltage range is required over several cycles. It further accelerates the side reaction with the electrolyte, and consequently cell performance is degraded.[32] For this reason, most LMR materials have been developed to have a small primary particle size, and it serves as a breaking point to increase the electrode density.
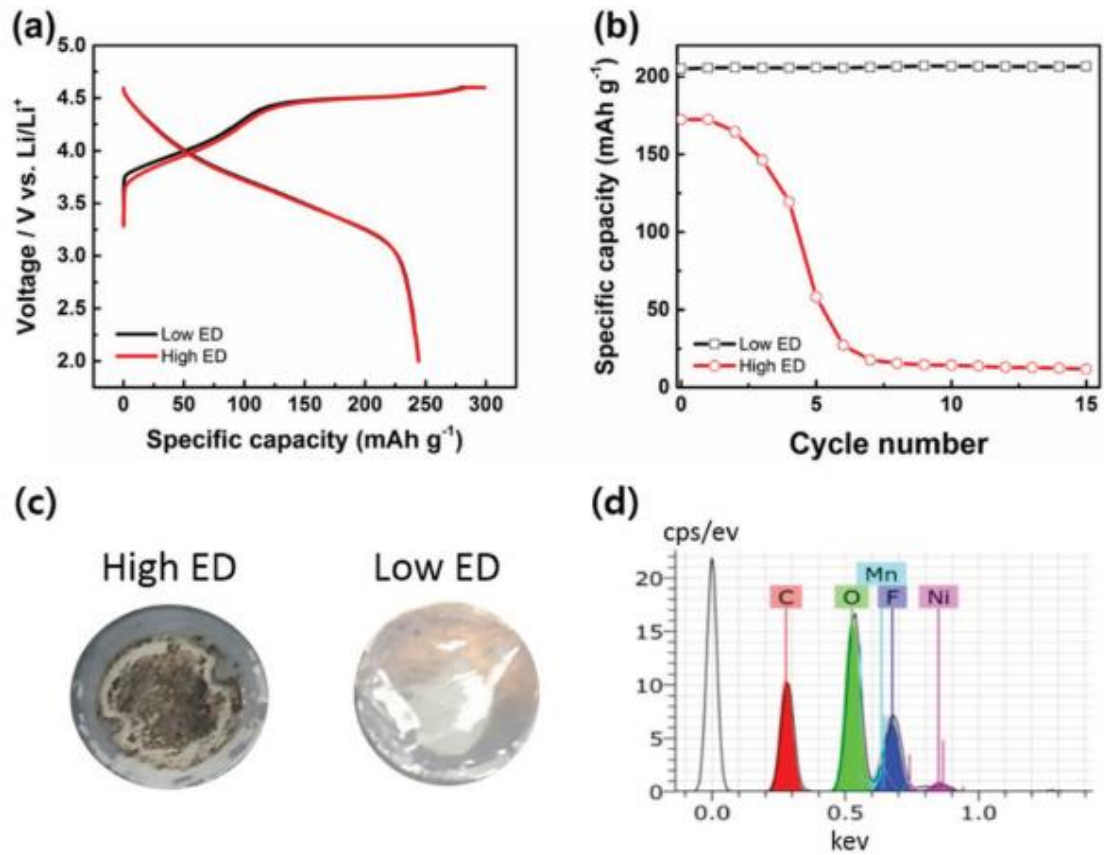
Figure 12. Electrochemical performance of LMR material with different electrode density in the voltage range of 2.0–4.6 V. (a) Initial charge/discharge profiles at C/10. (b) Cycling performance comparison of electrodes at C/2 charge and 1C discharge. (c) Photographs of the separator surfaces facing different anodes. (d) EDS spectrum of high density electrode separator.[12]

1.3.2 Side reactions with electrolyte at high operating voltage

Another challenging issue arises from the presence of Li_2MnO_3 phase and its activation process, which requires high operating voltage range above 4.4V. This voltage range is out of the electrochemical stability window of the electrolyte, and it accelerates the electrolyte decomposition. According to research about the relationship between operating voltage and the occurrence of pores and cracks inside the particle, as the upper cut-off voltage increases, the pore size becomes large and the number of crack increases. It should be noted that when the upper cut-off voltage is very high as 4.9V, not only the pore size is increased, but the cracks are interconnected from the surface to bulk space. As the internal region of the particles are exposed to the electrolyte directly, severe morphological degradation occurs in a large area.[29, 33, 34]

To make matters worse, in the case of LMRs, microstructural defects are formed more easily owing to the oxygen extraction during the initial cycles. It indicates that the rate at which the surface area in contact with the electrolyte widens is much faster than NCM cathode materials. This electrochemical property makes the structural stability of LMRs much lower than other cathode active materials. One research analyzed the change of structural displacement and strain of cathode materials according to the voltage range. LMRs begin to show the structural imperfection above 4.2V, and its degree is getting higher as the voltage is increased. At 4.4V, the point where voltage plateau regrading to the oxygen evolution is about to happen, the structural displacement and strain are generated more severely. To compare these phenomena with the conventional layered cathode, the same measurements were conducted for the $LiNi_{0.8}Co_{0.15}Al_{0.05}O_2$ (NCA). Obviously, dislocations are also formed at 4.2V in the NCA nanoparticles. As the voltage increases, however, no more discontinuity occurs. Likewise, the strains are calculated the maximum at 4.2V and it becomes lower with further charging. The changes of microstrain corresponding to the state of charge for LMR and NCA are represented in **Figure 13**. It contains additional analysis above 4.4V, and exhibits the same tendency as mentioned earlier. The occurrence of microstrain is increased gradually during the delithiation process for LMR. As further charged to higher voltage, additional dislocations as well as higher strains are induced. On the other hand, for the NCA, the incidence of microstrain reaches a peak at 4.2V, and it is gradually decreased.[15]
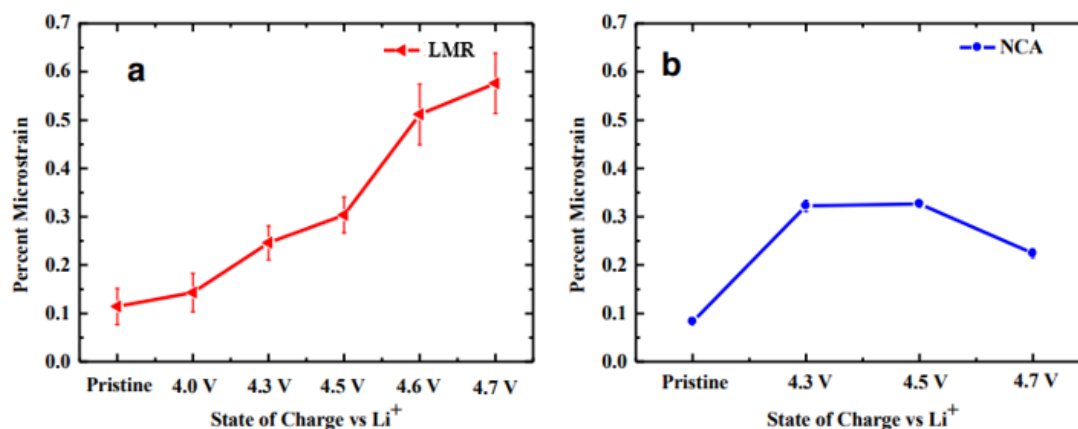
Figure 13. Comparison of microstrain changes for different states of charge of (a) LMR and (b) NCA, which is determined from the Williamson-Hall analysis of the Bragg peak widths from conventional X-ray diffraction experiments on a large number of particles. The data for LMR was measured *in situ*, while NCA was measured *ex situ*.[15]

It underpins that LMR has much lower structural stability when charging at high voltage than conventional layered oxide. Since LMRs have two different phases, $LiTMO_2$ and Li_2MnO_3, the lattice expansion generated during delithiation is partially confined until 4.4V. For this reason, the internal strain is greatly accumulated in LMRs, and exhibited by lattice displacement at micro-scales. It accelerates the irreversible structural rearrangement accompanied by the oxygen evolution in order to reduce the internal strain.[35-37] As a result, microcracks are easily formed, which enables electrolyte penetration and facilitates the particle degradation.

Figure 14 compares the states of LMR particles before and after 200 cycles. Non-cycled LMR cathode has layered structure, except for the spinel-like phase in a narrow area of the surface. Its secondary particle maintains its original morphology without any cracks. On the other hand, the cycled LMR cathode looks highly damaged. The surface of the secondary particle is pitted by the attack of HF, and non-uniform and a thick CEI layer is formed on the surface. As the byproducts generated by side reactions with the electrolyte are randomly stacked on the surface, intergranular microcracks have occurred during repeated cycles. Consequently, a new area is exposed to the electrolyte and side reactions happen more seriously. It leads to a large irreversible phase transformation, showing the formation of M_3O_4-spinel phase and $I4_1$ phase over a wide area in the bulk region.
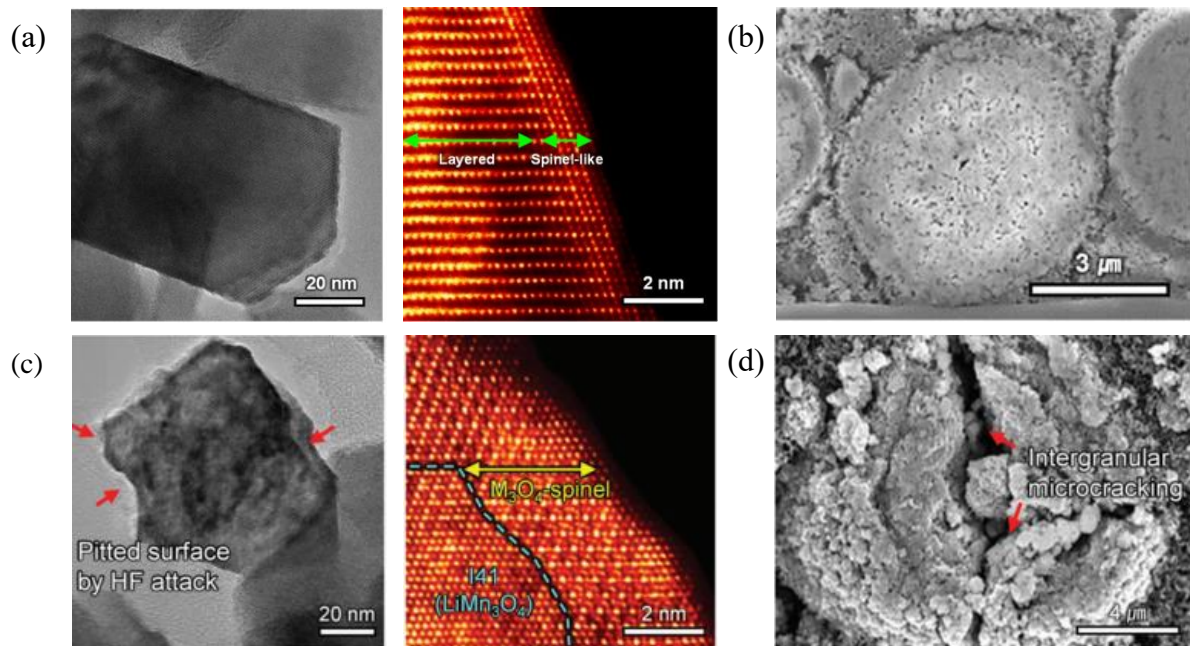
Figure 14. TEM and STEM images of (a) non-cycled and (c) cycled LMR cathode. Cross-sectional images of (b) non-cycled and (d) cycled LMR cathode.[11]

The reactions at the electrode-electrolyte interface are as follows. These equations represent the reactions for the decomposition of $LiPF_6$, which is the most commonly used as salt in the liquid electrolyte.

$LiPF_6 \rightarrow LiF + PF_5$

$PF_5 + H_2O \rightarrow POF_3 + 2HF$

$POF_3 + H_2O \rightarrow PO_2F + 2HF$

$PO_2F + H_2O \rightarrow H_3PO_4 + HF$
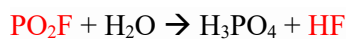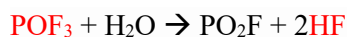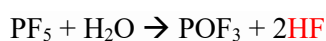
The undesirable HF generated from these reactions attacks the electrode, and F^- ions trigger metallic dissolution of Mn^{2+} and Ni^{2+}. $PO_xF_y^{z-}$ compounds also form a non-uniform and thick SEI layer, and destroy the interface.[38] All cathode materials have common problems in the occurrence of the side reactions with HF, and researches have been vigorously conducted to prevent it. The critical problem of LMRs is that there are additional side reactions that degrade the cell performance and structural stability.

$O_2 + e^- \rightarrow O_2\cdot^-$

$O_2\cdot^- + (CH_2O)_2CO$ (ethylene carbonate) $\rightarrow$ H_2O , CO_2 , CO, CO_3^{2-}

$O_2\cdot^- + 2CO_2 \rightarrow C_2O_6^{2-} + O_2$

$C_2O_6^{2-} + O_2\cdot^- + Li^+ + e^- \rightarrow Li_2CO_3, O_2$
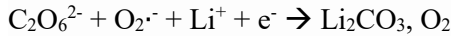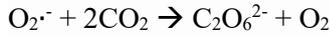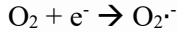
The following equations indicate the reactions caused by the release of oxygen, which particularly occur in the LMRs. As the extracted oxygen gas loses electrons, oxygen radicals are generated and they react easily with carbonated-based organic solvent to form byproducts, such as H_2O and CO_2. The generated H_2O is used as a source for the decomposition process of $LiPF_6$ to accelerate the reaction. In addition, CO_2 reacts with the oxygen radicals to generate $C_2O_6^{2-}$, which eventually becomes Li_2CO_3, a major component of the SEI layer.[10] A schematic diagram of this mechanism is summarized in **Figure 15**. Through it, it can be confirmed that the interfacial characteristics of LMRs accompanying the oxygen evolution make LMRs have more vulnerable structural instability and show high voltage decay.
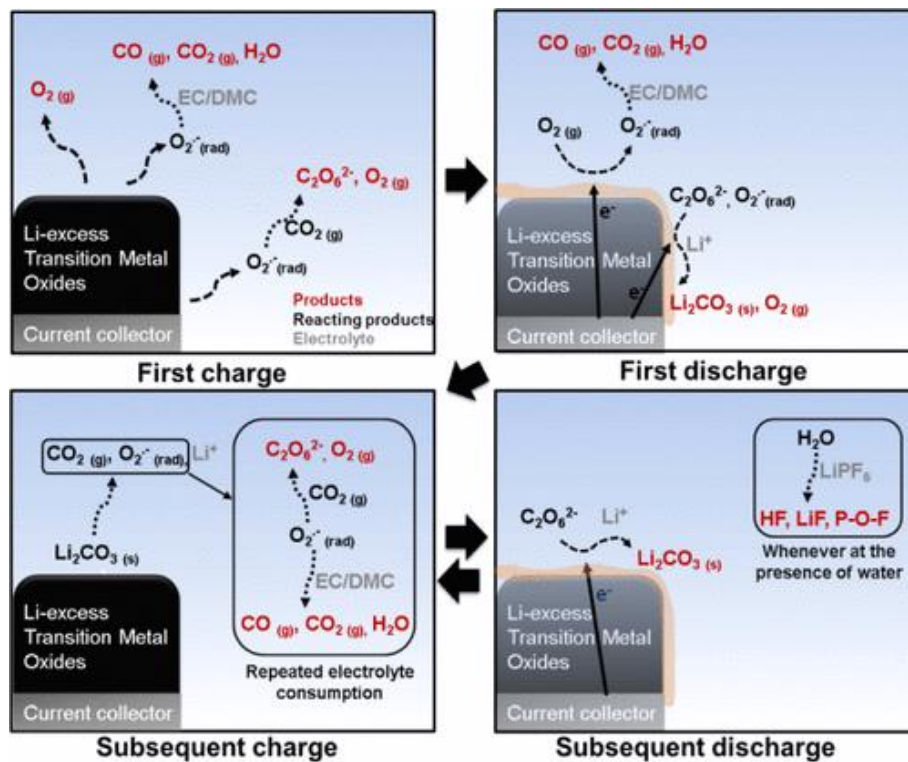
Figure 15. Scheme of the proposed mechanism of the successive reactions inside the closed system originated from the oxygen evolution out of the layered Li−excess metal oxides.[10]

1.4 Previous researches to improve the performance of LMRs

There has been a growing body of research that explores the appropriate method to solve intrinsic problems and practical challenges of LMRs, such as high initial irreversible capacity, severe voltage decay, low cycle stability, and poor rate capability. In recent years, outstanding enhancement have been realized with various strategies, including morphology and composition control during synthesis, surface modification, ion doping, development of electrolyte, and so on. From now on, we will review the previous researches regrading to the morphology control and surface coating, which are adopted in this work.

1.4.1 Morphology control during synthesis

Some researchers have sought to develop the morphology and structure of LMRs, which can achieve high volumetric energy density as well as superior electrochemical performance. Fu *et al.*[39] revealed that the morphology and structure of LMRs have a great influence on their electrochemical properties. By synthesizing LMRs with various morphologies, such as micro-sphere, micro-rods, nano-plates, and irregular particles, they found out that LMRs with the micro-rod shape showed the highest electrochemical performance among various morphologies. The micro-rod particles have an advantage of greatly improving the lithium ion diffusion with the one-directional lithium ion pathway. In addition, the nano-sized primary particles lower the energy barrier required for the lithium ion diffusion and their porous structure provides many reaction sites. With these properties of micro-rod particles, they showed better electrochemical performances than other shape of particles. However, there are also some challenges with its structure. The small particle size and porous structure increase the side reaction with the electrolyte, leading to the formation of the unstable and non-uniform SEI layer. Furthermore, as the phase transition accompanied by transition metal dissolution is propagated, the energy density is decreased severely during cycling. If increasing the particle size, the chemical activation of Li_2MnO_3 phase becomes difficult and the initial irreversible capacity is greatly increased. For the rapid activation, multiple cycles should be repeated at a high voltage range, which seriously affects the particle degradation. This reason has limited the increase in the particle size of LMR materials.

Oh *et al.*[8] proposed a new design of LMRs, where secondary particles are composed of large flake-type primary particles. The diameter of secondary particle size is nearly 10μm, and the length of primary particle inside is 1-3μm. The large primary particle size with a decreased surface area effectively alleviates the side reaction with the electrolyte. **Figure 16** shows the advantage of submicron-sized flake-type particles comparing with conventional nano-sized particles. Since the primary particles are well connected in one direction from the surface to the bulk site, they can show high lithium ion diffusivity, as mentioned in the previous paragraph as the benefit of rod-type morphology. At the same time, the decreased number of particles connected to the inside makes the resistance by the grain boundary much lower, leading to facile electronic conductivity. Even though high irreversibility is accompanied by the large particle size, this unique structure can facilitate the activation of Li_2MnO_3 phase with an effective activation process. This research suggested that LMRs can achieve high volumetric energy density and excellent electrochemical properties when they are synthesized with flake-type morphology and combined with an efficient activation process.
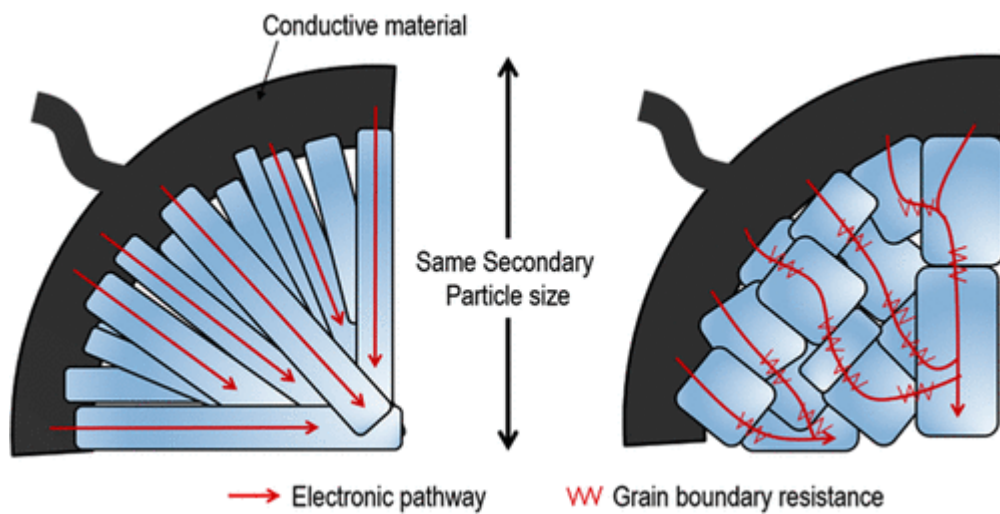
Figure 16. Schematic diagram showing electron migration through secondary particles composed of primary particles with different morphologies, either flake-shaped (left) or nanoparticle-shaped (right).[8]

1.4.2 Surface coating

Surface coating is one of the most important strategies applied to LMR cathode materials. There are some differences in the specific improvement depending on the coating materials, but the coating layer usually acts as a protective layer at the interface by preventing the excess oxygen evolution and mitigating side reactions with liquid electrolyte. These main functions of coating layer enable to improve the electrochemical properties of LMRs. Representative coating materials that have proven to be effective include metal oxide (Al_2O_3, MnO_2, MgO), metal phosphate ($AlPO_4$, $CoPO_4$), and metal fluoride (AlF_3, CoF_2, MgF_2). Wang et al.[40] reported that 3wt% Al_2O_3-coated $Li_{1.2}Ni_{0.13}Co_{0.13}Mn_{0.54}O_2$ showed higher specific capacity (253 mAhg^{-1} to 285mAhg^{-1}), which leads to the increased I.C.E (77% to 87%) at 0.05C. 2wt% $AlPO_4$ and 2wt% $CoPO_4$-coated samples also delivered the higher I.C.E of 91% and 84%, respectively. Moreover, rate capabilities are highly improved with the coating layer. Zou et al.[41] employed EIS analysis to compare the resistance of the uncoated and 3wt% Al_2O_3-coated sample. The result showed that the Al_2O_3-coated sample has a lower charge transfer resistance. It implies that the coating layer can effectively mitigate the formation of undesired SEI layers and enhance the electrochemical kinetics at the interface. Sun et al.[42] demonstrated that the AlF_3 coating layer not only alleviates the side reactions but also stabilizes the particle structure by suppressing the oxygen evolution at the surface. With these functions, the specific capacity of 3wt% AlF_3-coated $Li_{1.2}Ni_{0.17}Co_{0.07}Mn_{0.56}O_2$ is increased from 211 mAhg^{-1} to 225 mAhg^{-1}, and the capacity loss during 50 cycles is reduced from 105 mAhg^{-1} to 37 mAhg^{-1}. Zheng et al.[4] found out the detailed mechanism of the AlF_3 coating layer with STEM and EELS analysis. This study showed that AlF_3 coating made LMRs be activated considerably in the first cycle, triggering the surface reconstruction to the spinel-like phase. Even though the AlF_3 coating could not prevent phase transition completely, there was an obvious difference in the depth of the region where the structural transformation happened. Also, the AlF_3 coating acts as a buffer layer, thus it plays an important role in preventing the occurrence of corrosion caused by the side reactions with electrolyte. **Figure 17** illustrates the change of the particle structure of AlF_3-coated and uncoated samples during cycling. It simply shows the effective role of AlF_3 coating. All of these prior works have demonstrated that the surface coating enables LMRs to achieve better electrochemical properties. However, it is also notable that surface coating can sometimes lead to lower the electrochemical performance of LMRs.[39, 43, 44] Therefore, it is essential to identify all the different effects of coating materials and to select the most optimized ones.
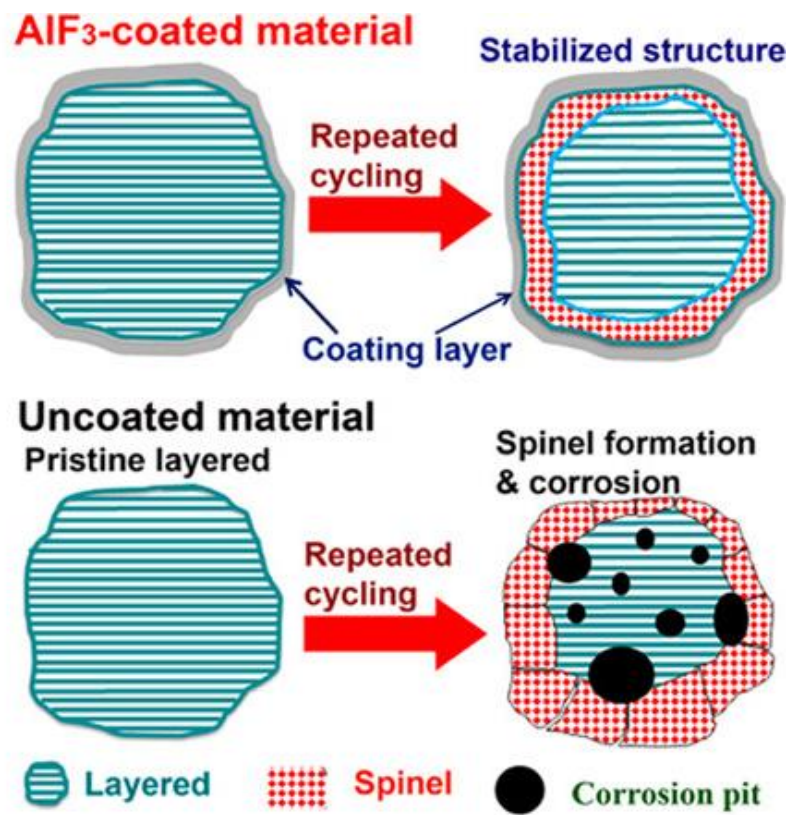
Figure 17. Schematic illustrations of the change of particle structure with and without AlF_3 coating during cycling.[4]

1.5 Objective in the works

In spite of the superior theoretical specific capacity of LMRs, their commercialization has been hindered by low volumetric energy density and several inferior electrochemical properties of LMRs. In order to resolve several problems of LMRs at the same time, a new approach is necessary. Herein, two different methods are introduced to LMRs simultaneously: morphology control during the co-precipitation process and surface modification. First of all, we synthesized flake-type LMRs with the large primary particle size by controlling various conditions, such as gas flow rate, pH, temperature, and reaction time. Generally synthesized LMRs are composed of spherical-type particles with small particle size and have porous structure, which result in low volumetric energy density. By comparing the electrochemical evaluation with this conventional spherical-type LMRs, the effect of flake-type morphology with large particle size was demonstrated in this work. Also, GITT test was carried out to find out the main reason for the capacity fading and voltage decay. In order to enhance the irreversibility caused by the trade-off relationship with increased particle size, surface coating should be followed as the second procedure. Aluminium fluoride (AlF_3), one of the most promising coating materials among various coating materials (phosphates, fluorides, metal oxides, etc.), was adopted for the synthesized LMRs. Through the electrochemical evaluation and structural analysis with TEM, we revealed that how the AlF_3 coating changes the pristine particle structure and how the process of phase transition is changed during the cycles. EIS test was conducted together to understand the mechanism for the results. By demonstrating the various effects of the method proposed in this study, we suggest that AlF_3-coated Li-, Mn- rich cathode materials, whose morphology is controlled by flake-type, are able to be next-generation cathode materials. Furthermore, this work can support that LMRs can be sufficiently developed as cathode materials introduced into EVs and ESSs in the near future.

II. Experimental section

Material preparation

Preparation of pristine sample: $Mn_{0.75}Ni_{0.25}(OH)_2$ precursor was obtained by a co-precipitation method. $NiSO_4 \cdot 6H_2O$ and $MnSO_4 \cdot 5H_2O$ were dissolved in distilled water at 2M concentration with molar ratio Mn:Ni = 3:1. 4M NaOH solution and 6M NH_4OH solution for chelating were also prepared, respectively. Each solution was flowing into 5L continuous stirred tank reactor (CSTR) under N_2 atmosphere, and mixed for 20 hours at 50℃. The pH condition was adjusted to 10.5 by controlling the feeding rate of NH_4OH solution. The $Mn_{0.75}Ni_{0.25}(OH)_2$ precursor was finally obtained after repeating washing and filtering process over ten times, and drying at 120℃ overnight. The synthesized hydroxide precursor was first calcined at 600℃ for 5 hours to be oxide precursor. Then, it was mixed with LiOH with Li/TM ratio = 1.5, preheated at 450℃ for 5 hours and annealed at 960℃ for 10 hours in the air to obtain $Li_{1.2}Mn_{0.6}Ni_{0.2}O_2$.

Coating method: $Al(NO_3)_3$ and NH_4F were diluted with distilled water separately with the molar ratio Al:F=1:3. In the $Al(NO_3)_3$ solution, pristine $Li_{1.2}Mn_{0.6}Ni_{0.2}O_2$ sample was immersed at first and stirred at 50℃. Then, NH_4F solution was slowly added. Total solution was stirred vigorously while maintaining the temperature at 80℃ for 5 hours. The designed amount of AlF_3 was 1, 2, 3 and 5wt% of $Li_{1.2}Mn_{0.6}Ni_{0.2}O_2$ powder. When the reaction time was over and the solvent evaporated enough, the product was completely dried in a 120℃ oven. With calcination at 450℃ for 5 hours in N_2 atmosphere, AlF_3-coated sample was finally obtained.

Electrochemical characterization

All the electrochemical evaluations were performed with 2032R coin-type half cells at room temperature (25℃) using a battery cycler (WBVS-3000, Wonatech). The positive electrode was prepared through the slurry casting process with 95% of cathode active materials, 3% of poly(vinylidene fluoride) binder, and 2% of carbon nanotube (CNT, Cnano) dissolved in N-methyl-2-pyrrolidone (NMP). The obtained slurry was casted onto the 30μm aluminium foil with the loading level of 5.5~6mg cm^{-2}, then roll-pressing was carried out to make the electrode density around 3g cm^{-3}. The electrodes were dried in a vacuum oven at 120℃ for 10 hours. With the lithium metal as a negative electrode, the prepared positive electrode was assembled to coin-type half cells in an argon-filled glove box. 1.3M $LiPF_6$ in ethylene carbonate (EC), ethyl methyl carbonate (EMC), and dimethyl carbonate (DMC) (3:4:4,

v/v/v) was used for an electrolyte, and polyethylene (Celgard) microporous polymer was used for a separator.

The electrochemical performance was carried out at the constant charge/discharge C-rate of 0.2C in the voltage range of 2.5-4.7V for the first cycle, and 2.5-4.6V for the second cycle. After two formation cycles, the long-term cycle test was performed at 2.5-4.6V with charge/discharge C-rate of 1C. Rate capabilities were measured with charge C-rate of 0.2C and different discharge C-rates of 0.2/ 0.5/ 1/ 2/ 3C, where three cycles were repeated at each discharge C-rate. The galvanostatic intermittent titration technique (GITT) was performed at constant C-rate of 1C for 6 min with a resting time for 3 hours in the voltage range 2.0-4.8V. The EIS test was carried out with frequency range from 1MHz to 10MHz and a DC voltage amplitude of 10mV after fully charged to 4.6V.

Material characterization

In order to observe the cross-sectioned images of cathode materials, an ion milling system (Model 1040 Nanomill, Fischione) was used. The ion-milled electrode and the morphology of the cathode powder were analyzed by scanning electron microscopy (SEM, Verios 460, FEI) attached with energy dispersive X-ray spectroscopy (EDX, XFlash® 6130, Bruker). The crystallographic structure of the materials was investigated by X-ray diffraction (XRD) patterns using an X-ray diffractometer (Rigaku D/MAX 2500 V/PC) with Cu-Kα radiation. A scan range was from 10° to 80° (2 theta) with a scan step of 0.02° and a counting time of 5 s. High resolution transmission electron microscopy (HR-TEM, ARM300, JEOL) was operated for the structural and elemental analysis in the atomic-scale. For TEM sampling, cross-sectioned samples were prepared by dual-beam focused ion beam (FIB, Helios 450HP, FEI). Scanning transmission electron microscopy (STEM) images, energy dispersive X-ray spectroscopy (EDX), and electron energy loss (EELS) were obtained from it.

III. Result and Discussion

3.1 Flake-type Co-free LMR cathode materials for high-energy density

The secondary particles of Li-, Mn-rich cathodes (LMRs) are generally composed of small primary particles with spherical-type morphology, which causes the problems of poor cycling performance and low volumetric energy density. In order to solve them, we synthesized the flake-type hydroxide precursor with a large primary particle size by controlling experimental conditions during the co-precipitation process. When the size of the primary particles is simply increased maintaining the spherical shape, the full activation of Li_2MnO_3 phases becomes delayed. It results in a significant increase in irreversible capacity. On the other hand, flake-type morphology can solve this problem by reducing the resistance by grain boundaries. That is to say, the flake-type shape can improve the electronic conductivity and lithium ion diffusivity, and eventually solve the problems of partial activation as well as low volumetric energy density.

Figure 18 shows cross-sectioned SEM images of the flake-type $Mn_{0.75}Ni_{0.25}(OH)_2$ precursor obtained by co-precipitation and the oxide precursor obtained after the first calcination at 600°C for 5 hours, respectively. It confirms that primary particles grew in an outward direction with a flake-type shape inside the secondary particles during the co-precipitation process. From XRD analysis, peaks of $Mn(OH)_2$ and $Ni(OH)_2$ were observed in the hydroxide precursor. In the oxide precursor, the peaks were well matched with those of Mn_3O_4 and NiO (**Figure 19**). Through lithiation at 960°C for 10 hours, $Li_{1.2}Mn_{0.6}Ni_{0.2}O_2$ (denoted as MN7525) cathode active material was obtained. As shown in **Figure 20a**, MN7525 maintained a flake-type shape and its particle size became larger due to the insertion of lithium ions. **Figure 20b** shows a TEM image of MN7525 primary particle, and its higher magnification TEM image of the surface is shown in **Figure 20c**. The fast Fourier transform(FFT) patterns of the site I and site II indicate that it has the layered structure throughout the particle (**Figure 20d**).

(a)

3 μm

(b)

$3\,\mu m$
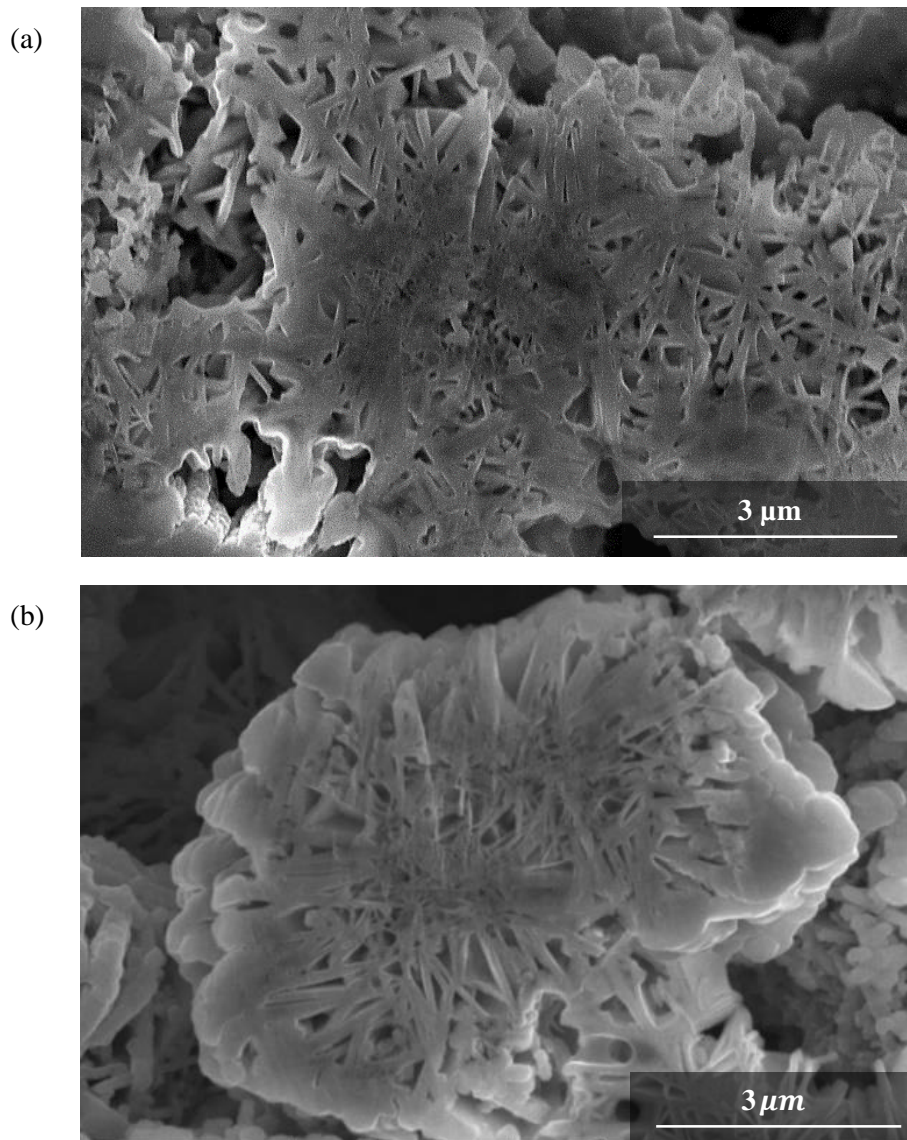
Figure 18. Cross-sectioned SEM images of (a) flake-type $Mn_{0.75}Ni_{0.25}(OH)_2$ precursor obtained from co-precipitation, and (b) oxide precursor after 1st calcination at 600°C.
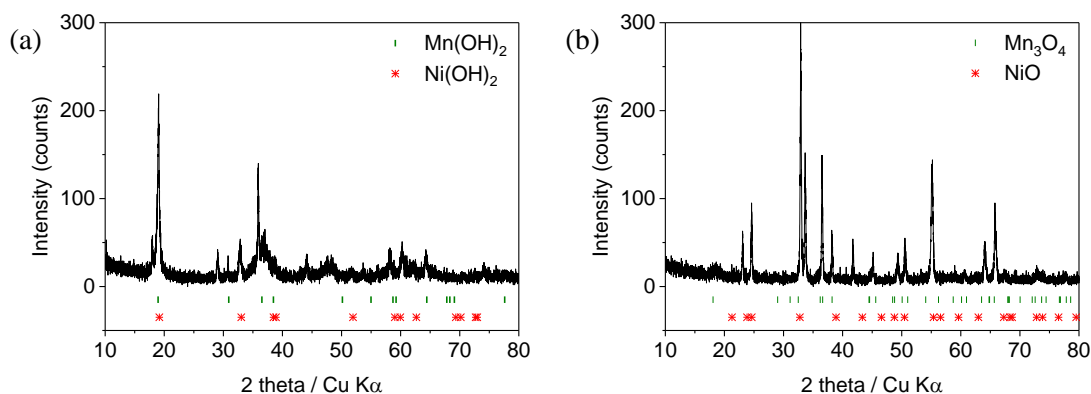
Figure 19. X-ray diffraction (XRD) patterns of (a) flake-type $Mn_{0.75}Ni_{0.25}(OH)_2$ precursor obtained from co-precipitation, and (b) oxide precursor after 1st calcination at 600°C.

In order to investigate the improved cell performance of the LMR material having a flake-type morphology, electrochemical evaluation of MN7525 was conducted together with conventionally synthesized LMRs with a spherical-type shape. $Li_{0.15}Mn_{0.51}Ni_{0.17}Co_{0.17}O_2$ (denoted as MNC622) was used for comparison. The morphology of flake-type MN7525 and spherical-type MNC622 can be seen in **Figure 21**. Although MN7525 and MNC622 have completely different morphologies, the XRD patterns in **Figure 22** indicate that both LMR samples are Li-excess materials, which have super-lattice structures. Rietveld refinement was also conducted for these XRD patterns, and lattice constants and structure parameters were summarized in **Tables 1** and **2**, respectively. According to these results, it was demonstrated that lithium ions exist in the transition metal layer in both MN7525 and MNC622. The presence of Li_2MnO_3 phase was clearly verified.

(a)

(b)

(c)

(d)   Site I   Site II
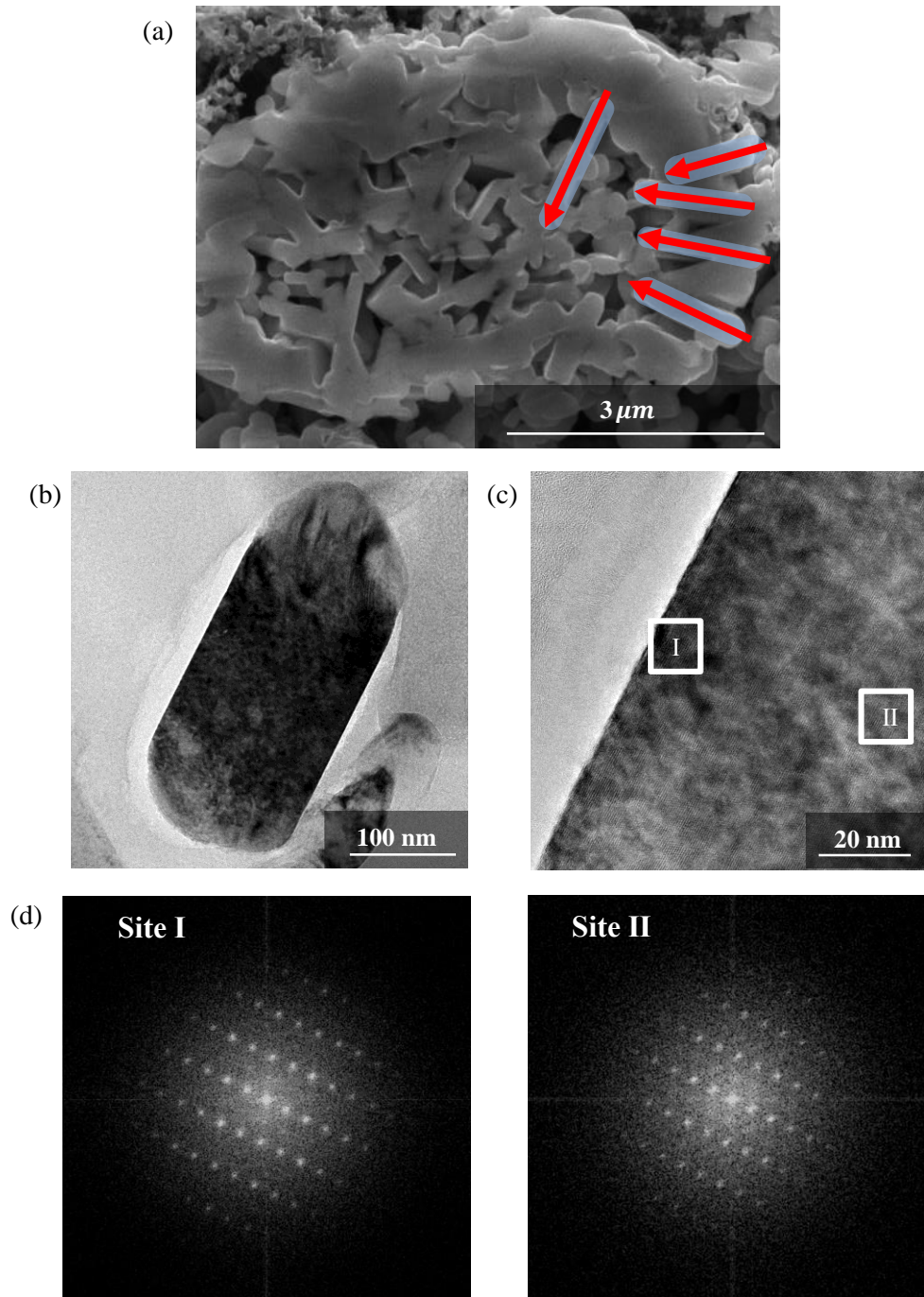
Figure 20. (a) Cross-sectioned SEM images of $Li_{1.2}Mn_{0.6}Ni_{0.2}O_2$. (b) Overall view of TEM image showing pristine MN7525 particle and (c) higher magnification TEM image showing its surface. (d) Fast Fourier transform patterns of outer site I and inner site II.

(a) $Li_{1.2}Mn_{0.6}Ni_{0.2}O_2$ (MN7525)

(b) $Li_{1.15}Mn_{0.51}Ni_{0.17}Co_{0.17}O_2$ (MNC622)
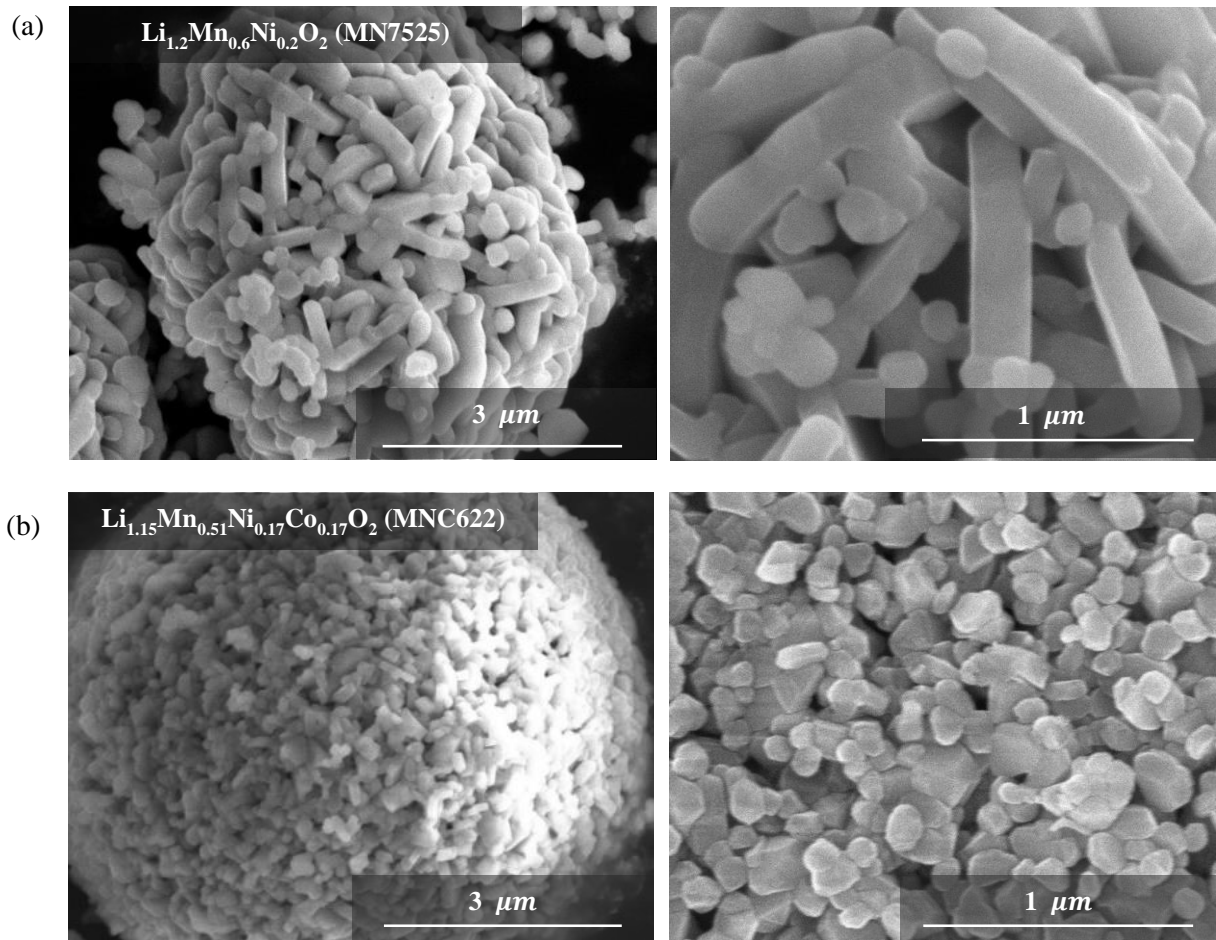
Figure 21. Morphological information for MN7525 and MNC622. SEM images of (a) flake-type MN7525 and (b) spherical-type MNC622.

28
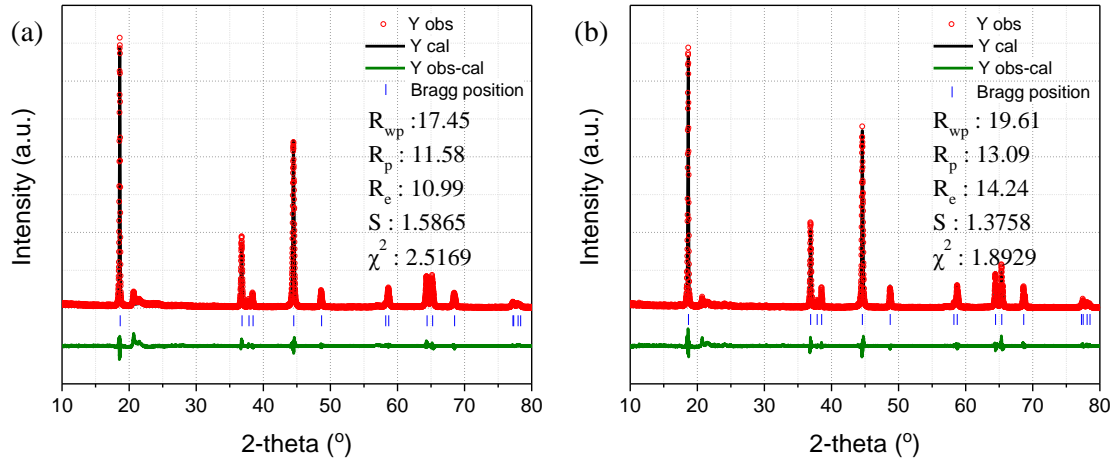
Figure 22. X-ray diffraction (XRD) pattern and Rietveld refinement of pristine (a) MN7525 and (b) MNC622 powder.

Sample	a(A)	c(A)	c/a	V(A^3)	Strain(%)
MN7525	2.85822(18)	14.2440(12)	4.9835	100.776(23)	0.199(7)
MNC622	2.85268(15)	14.2429(9)	4.9928	100.377(10)	0.073(4)

Table 1. Lattice constants for pristine MN7525 and MNC622.

MN7525

Element	X	Y	Z	Occupancy
Li	0.000000	0.000000	0.000000	0.939(3)
Ni	0.000000	0.000000	0.000000	0.061(3)
O	0.000000	0.000000	0.241100	1.000
Mn	0.000000	0.000000	0.500000	0.600
Ni	0.000000	0.000000	0.500000	0.139(3)
Li	0.000000	0.000000	0.500000	0.261(3)

MNC622

Element	X	Y	Z	Occupancy
Li	0.000000	0.000000	0.000000	0.900(3)
Ni	0.000000	0.000000	0.000000	0.100(3)
Co	0.000000	0.000000	0.000000	0.002(5)
O	0.000000	0.000000	0.241100	1.000
Mn	0.000000	0.000000	0.500000	0.510
Ni	0.000000	0.000000	0.500000	0.100(3)
Co	0.000000	0.000000	0.500000	0.168(5)
Li	0.000000	0.000000	0.500000	0.200(3)

Table 2. Structure parameters for pristine MN7525 and MNC622.

Figure 23 shows the voltage profiles of MN7525 and MNC622 in the first charge/discharge cycle. Since MN7525 is Co-free and has a higher Mn ratio, the proportion of Li_2MnO_3 phase occupied is higher than MNC622. In addition, the large particle size makes the full activation of Li_2MnO_3 phase difficult. Thus, the voltage plateau around 4.4V is lengthened in the initial charging process, resulting in low I.C.E. The initial charge capacity of MN7525 is 345.6mAh/g, and the I.C.E is 72.8%. Considering the initial charge capacity of MNC622 is 295.2mAh/g, and the I.C.E is 75.0%, MN7525 shows higher irreversible capacity. When comparing the initial discharge capacities, however, the capacity of MN7525 is increased by approximately 30mAh/g than that of MNC622. It is worth noting that the flake-type morphology achieves a remarkable improvement in cycle stability. The capacity retention during the cycle is approximately 96%, which is 2% higher than MNC622. The average voltage decay is 0.045V after 40 cycles. Comparing with the voltage decay of MNC622, the value of voltage drop is reduced by almost half (**Figure 24**). These results demonstrate that Co-free LMRs with flake-type morphology can significantly improve low cycle stability and high voltage decay by irreversible degradation, which are considered as the big problems of conventional LMRs.
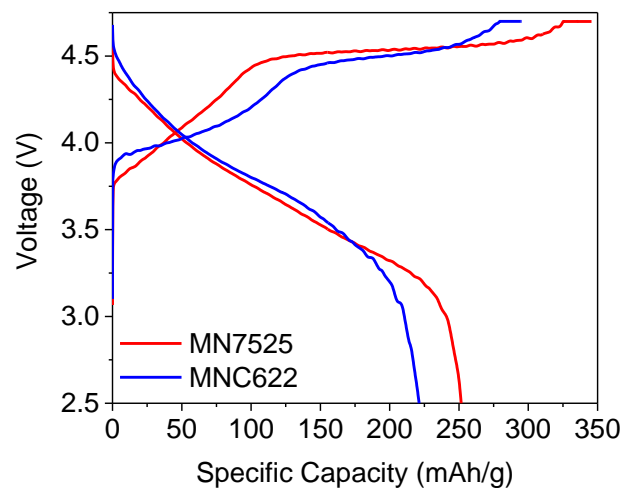
Figure 23. Voltage profiles of MN7525 and MNC622 in the range of 2.5-4.7V at 0.2C.

Samples	1st Charge capacity (mAh/g)	1st Discharge capacity (mAh/g)	Initial Coulombic Efficiency (%)
MN7525	345.6	251.6	72.8
MNC622	295.2	221.3	75.0

Table 3. Initial charge/discharge capacity, Coulombic efficiency of MN7525 and MNC622

Through the comparison of voltage profiles during the cycles, the same results can be derived. **Figure 25** shows the voltage profile of two samples from the first cycle to the 40th cycle at 1C charge/discharge after two formation cycles. MN7525 shows little change over the cycles. It means it has high cycling stability. On the other hand, in the case of MNC622, the profile is gradually shifted to lower voltage due to high overpotential. It is the reason for the high voltage decay of MNC622.

Samples	Capacity retention (%)	Voltage decay (V)
MN7525	95.9	0.045
MNC622	94.0	0.086
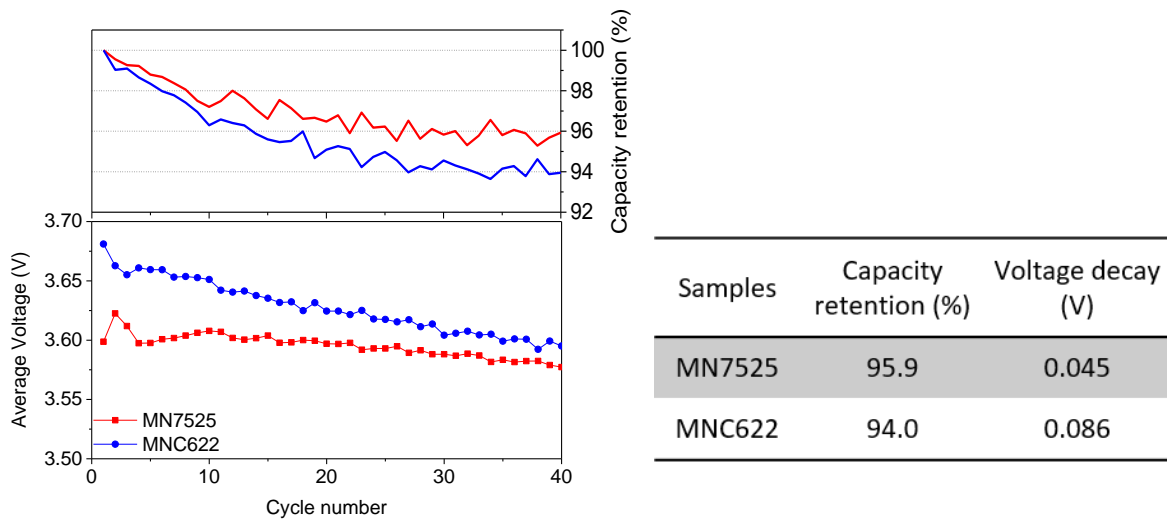
Figure 24. Discharge capacity retention and average voltage of MN7525 and MNC622 as a function of the number of cycles between 2.5 and 4.6V at 1C.
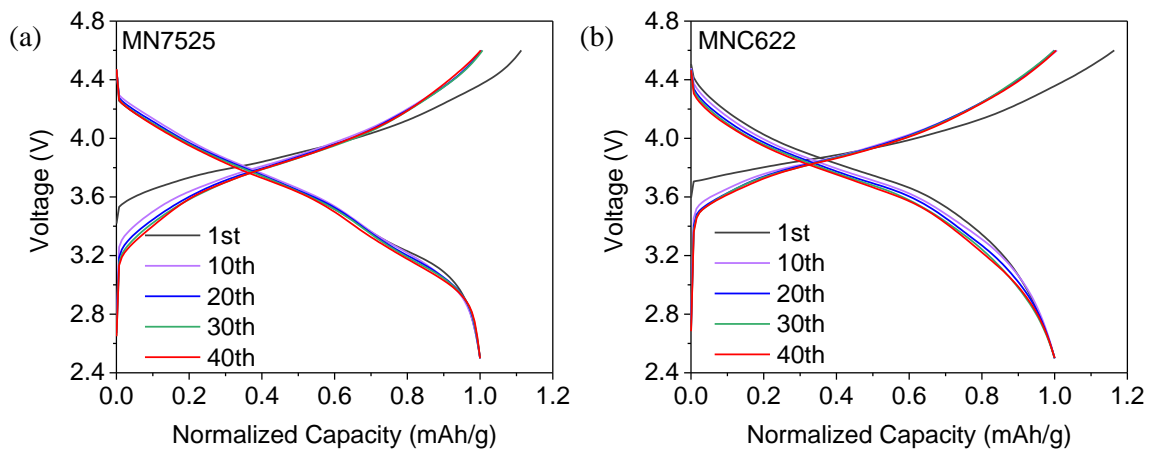
Figure 25. Voltage profiles of (a) MN7525 and (b) MNC622 at the 1st, 10th, 20th, 30th, and 40th cycle with 1C after two formation cycles.

The flake-type primary particle shape has the advantage of improving rate capability as well as cycling performance. The result of rate capability test is shown in **Figure 26**. When the C-rate is 0.2C, the capacity difference between the two samples is about 25mAh/g. However, this gap is greatly increased to 50mAh/g as the C-rate is increased to 3C. In order to analyze this phenomenon in more detail, an electrochemical GITT analysis was conducted for MN7525 and MNC622. **Figure 27** shows the voltage profile obtained from GITT for each sample before and after 40 cycles in voltage range 2.0V-4.8V.
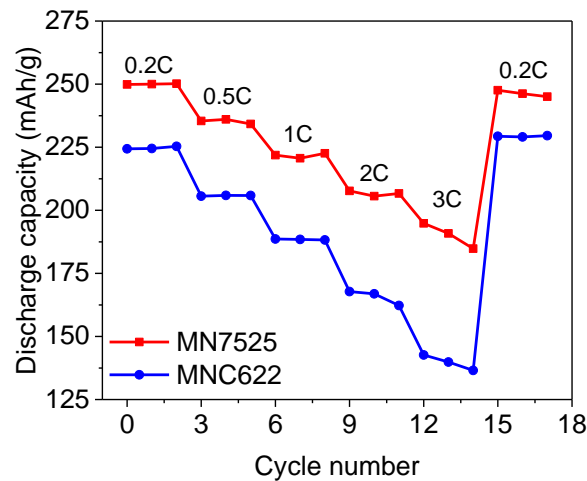
Figure 26. Rate capabilities of MN7525 and MNC622 in voltage range 2.5-4.6V.
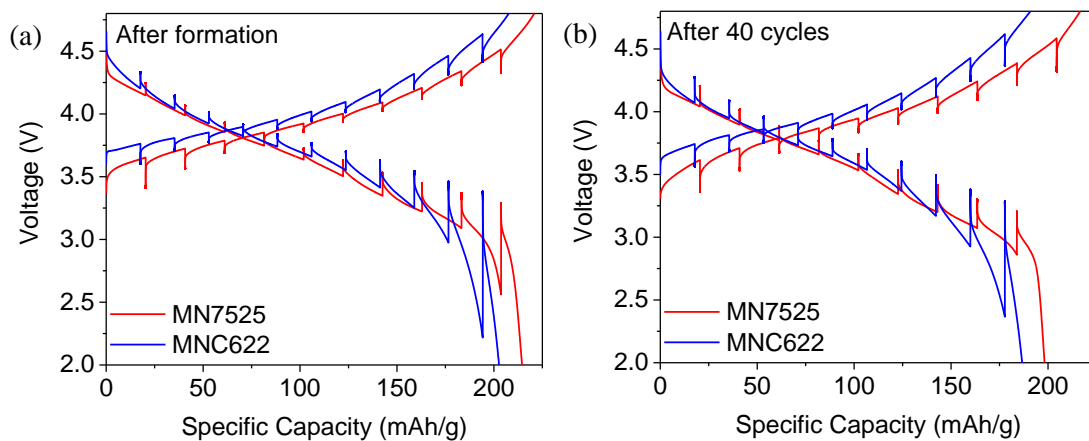
Figure 27. Voltage profiles obtained from the galvanostatic intermittent titration technique (GITT) of MN7525 and MNC622 after (a) formation and (b) 40 cycles.

The result of analyzing the overpotential according to each depth of discharge (DOD) is shown in **Figure 28**. The overpotential of MN7525 is lower in most of the discharge states, regardless of before and after cycling. As the DOD increases, the gap of overpotential between two samples gradually increases. As the DOD is more that 80%, it shows a particularly sharp difference. Even when the overpotential is divided into ohmic voltage loss, so-called IR drop, and non-ohmic voltage loss, all numerical values are calculated higher in MNC622.
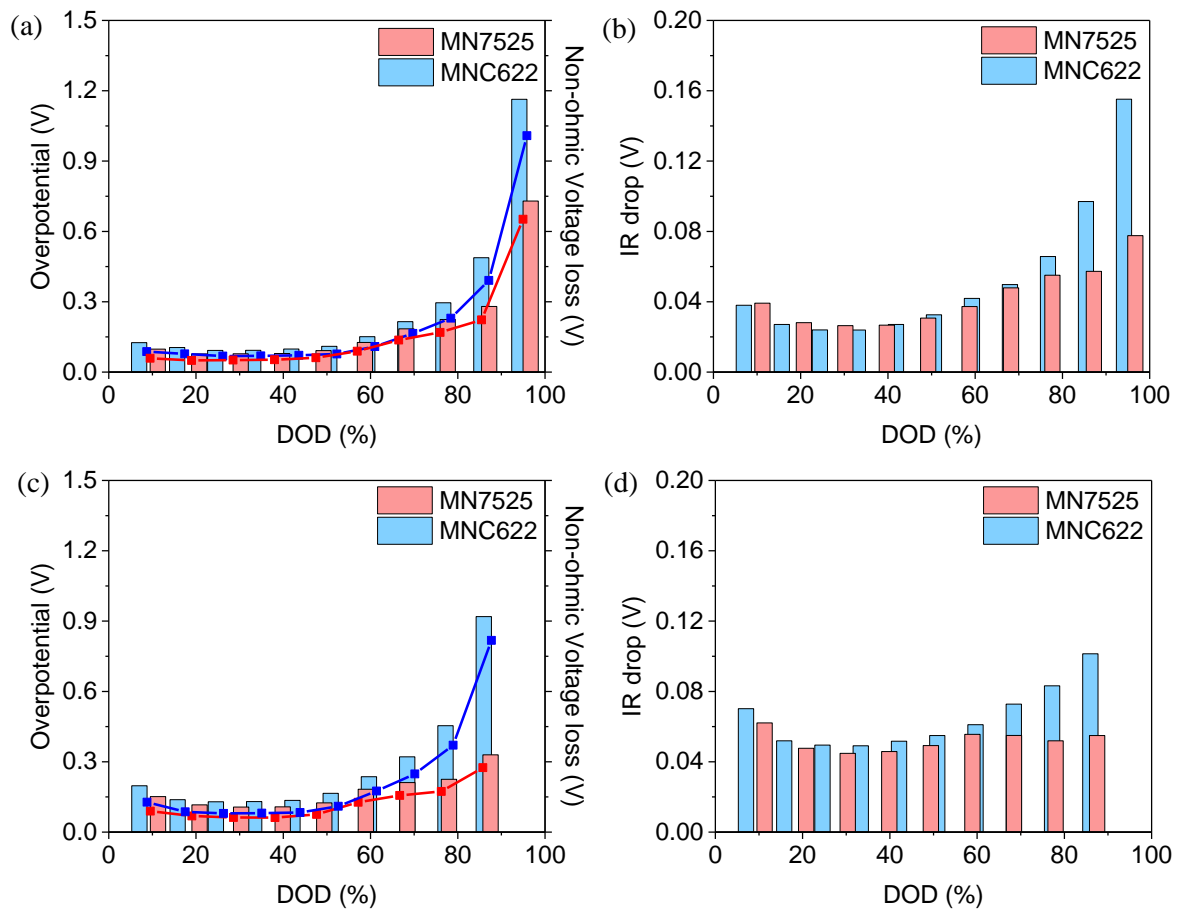
Figure 28. Overpotential, non-ohmic voltage loss, and IR drop calculated from the galvanostatic intermittent titration technique (GITT) (a),(b) after formation and (c),(d) after 40 cycles.

The first point to note here is that the non-ohmic voltage loss occupies most of the overpotential, as shown in **Figures 28a** and **28c**. Non-ohmic voltage loss is mainly caused by the resistance from phase transition. The flake-type primary particles have relatively large particle size, thereby the surface area exposed to the electrolyte is small. On the other hand, the spherical-type particles have a wide surface area where side reactions with an electrolyte occur a lot. A thick SEI is formed, and it makes the microcracks in the secondary particles being generated more easily. Since side reactions happen actively with a relatively wide contact area, it can be predicted that structural evolution occurs to a great extent in MNC622. As a result, as shown in **Figure 28c**, the value of non-ohmic voltage loss of MNC622 after cycling is significantly higher than that of MN7525. Their gap between two samples is more pronounced compared to that before cycling.

Second, when analyzing the IR drop of each sample (**Figure 28b, 28d**), MNC622 shows higher IR drop. It implies that electronic resistance occurs greatly in MNC622. The secondary particles of MNC622 and MN7525 have similar diameters of approximately 10μm, as shown in **Figure 29**. However, the movement of electrons is highly disturbed in the secondary particles composed of the small spherical-type primary particles. This is because there is a large number of grain boundaries present in the movement of electrons from the surface of the particles to the inside. The resistance caused by the grain boundaries can be reduced with the flake-type primary particles as the number of primary particles that electrons are required to move through is decreased. It leads to high electronic conductivity and lithium ion diffusivity. As a result, it enables the flake-type MN7525 to exhibit high rate capability as well as excellent cycle retention.
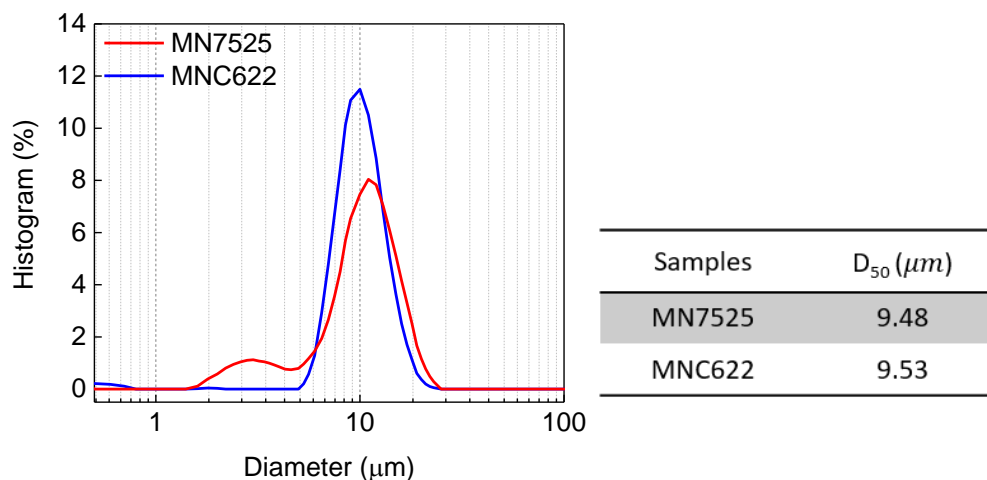
Figure 29. Particle size distribution analysis of MN7525 and MNC622.

By comparing the lithiation/delithiation process occurring in a secondary particle composed of flake-type and spherical-type, the advantages of flake-type morphology can be clearly identified. To sum up, the LMR active materials with flake-type primary particles have two main advantages. At first, the occurrence of side reactions with liquid electrolyte can be diminished. This is because flake-type particles have larger particle size and a smaller surface area that contacts with electrolyte. It results in lowering the formation of thick SEI layer and microcracks, and eventually the occurrence of phase transformation. As discussed in GITT analysis, the non-ohmic voltage loss during the cycles is greatly reduced in particular. It indicates that the voltage decay generated by phase transition is highly decreased, thereby low voltage decay and improved cycling performance can be achieved. Second, the electronic conductivity is enhanced with the decreased number of grain boundaries inside the secondary particles. Since the number of primary particles connected to the inside of the particles is small, it is easy for electrons to move from the surface to the inside. As a result, the charge transfer resistance is lowered, and the rate capability is enhanced. To sum up, morphology control with flake-type primary particles enables not only to increase the volumetric energy density, but to improve the electrochemical properties such as cycle performances and rate capabilities, which are considered as practical challenges of LMR cathodes.

3.2 AlF$_3$ surface coating for high-performance LMR cathode materials

The fundamental reason for the large irreversible capacity occurring in the initial cycles is a presence of Li$_2$MnO$_3$ phase with high crystallinity. The Li$_2$MnO$_3$ phase is electrochemically activated above 4.4 V during several initial charge/discharge cycles gradually. With the flake-type morphology, I.C.E is further reduced due to the large primary particle size. This is because it becomes more difficult to activate the Li$_2$MnO$_3$ phase completely as the particle size increases. Therefore, activating the Li$_2$MnO$_3$ phase in advance by applying the chemical activation process to LMRs can be a good method to decrease the irreversible capacity occurring in the first cycle. However, there is a problem that excess amount of lithium ions and O$_2$ gas are generated from the surface of the LMR material during the Li$_2$MnO$_3$ activation process. It not only accelerates the side reactions with the electrolyte to form thick SEI layer, but also promotes phase transformation at the interfaces. For this reason, irreversible degradation during the cycle happens more severely in the LMRs, and they are hindered from realizing and maintaining high volumetric energy density.

Therefore, a post-treatment process that leads to rapid activation of Li$_2$MnO$_3$ phase as well as stabilizes the surface is required. Aluminum fluoride (AlF$_3$) is one of the most suitable coating materials in this perspective. Herein, the surface modification with AlF$_3$ was introduced. A pristine MN7525 cathode active material was used as an uncoated sample and AlF$_3$ coating was applied to a pristine sample to prove its effects. **Figure 30** shows the results of XRD analysis of uncoated and 1, 3, and 5wt% AlF$_3$-coated samples. Three monoclinic peaks, $(020)_M$, $(110)_M$, and $(111)_M$, between 20° and 25°, are well observed in all samples, which indicates a layered structure with honeycomb orderings of LiTMO$_2$ and super-lattice structure of Li$_2$MnO$_3$. Although the peak intensities of the AlF$_3$-coated samples are slightly reduced, the structure of the cathode material does not significantly change during the AlF$_3$ coating process. Rietveld analysis also shows that the lithium ions are present in the transition metal layer, verifying the Li-excess structure is well maintained (**Table 4**).
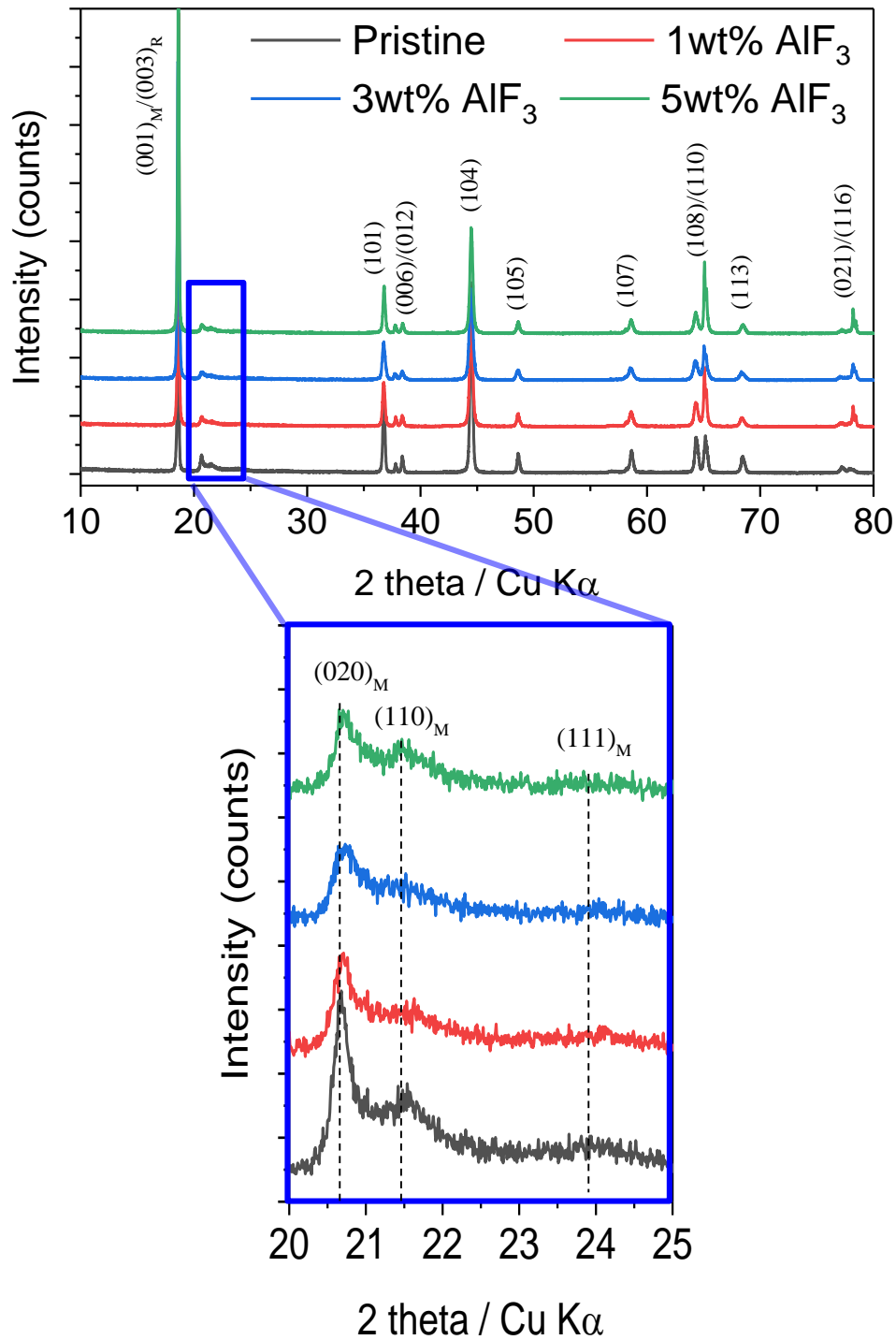
Figure 30. X-ray diffraction (XRD) patterns of pristine and AlF_3-coated (1,3,5wt%) LMR samples with an enlargement of peaks at $2\theta=20\text{-}25°$ on the right.

1wt% AlF₃ coated

Element	X	Y	Z	Occupancy
Li	0.000000	0.000000	0.000000	0.970(2)
Ni	0.000000	0.000000	0.000000	0.030(2)
O	0.000000	0.000000	0.241100	1.000
Mn	0.000000	0.000000	0.500000	0.600
Ni	0.000000	0.000000	0.500000	0.170(2)
Li	0.000000	0.000000	0.500000	0.230(2)

3wt% AlF₃ coated

Element	X	Y	Z	Occupancy
Li	0.000000	0.000000	0.000000	0.9817(18)
Ni	0.000000	0.000000	0.000000	0.0183(18)
O	0.000000	0.000000	0.241100	1.000
Mn	0.000000	0.000000	0.500000	0.600
Ni	0.000000	0.000000	0.500000	0.182(18)
Li	0.000000	0.000000	0.500000	0.218(18)

5wt% AlF₃ coated

Element	X	Y	Z	Occupancy
Li	0.000000	0.000000	0.000000	0.984(2)
Ni	0.000000	0.000000	0.000000	0.016(2)
O	0.000000	0.000000	0.241100	1.000
Mn	0.000000	0.000000	0.500000	0.600
Ni	0.000000	0.000000	0.500000	0.184(2)
Li	0.000000	0.000000	0.500000	0.216(2)

Table 4. Structure Parameters for 1, 3, 5wt% AlF_3-coated LMR samples.

Figure 31 shows SEM-EDS analysis and mapping images on the surface of the secondary particles for 3wt% AlF_3-coated samples. At the surface, both the Al peak and F peak are well observed. By analyzing the cross-sectioned primary particle through TEM-EDS mapping (**Figure 32**), it is confirmed that an AlF_3 coating layer is formed on the surface of the primary particle. According to 3wt% AlF_3-coated samples, the thickness of the coating layer is about 4-5nm. The result of TEM-EDS line scanning also demonstrates that Al and F exist on the surface of the particles. Although the peak intensity is far smaller than that of Mn, Ni, and O, it can be seen that the particles are well coated with AlF_3 on the surface when comparing with the intensity in the internal region (**Figure 32b**).
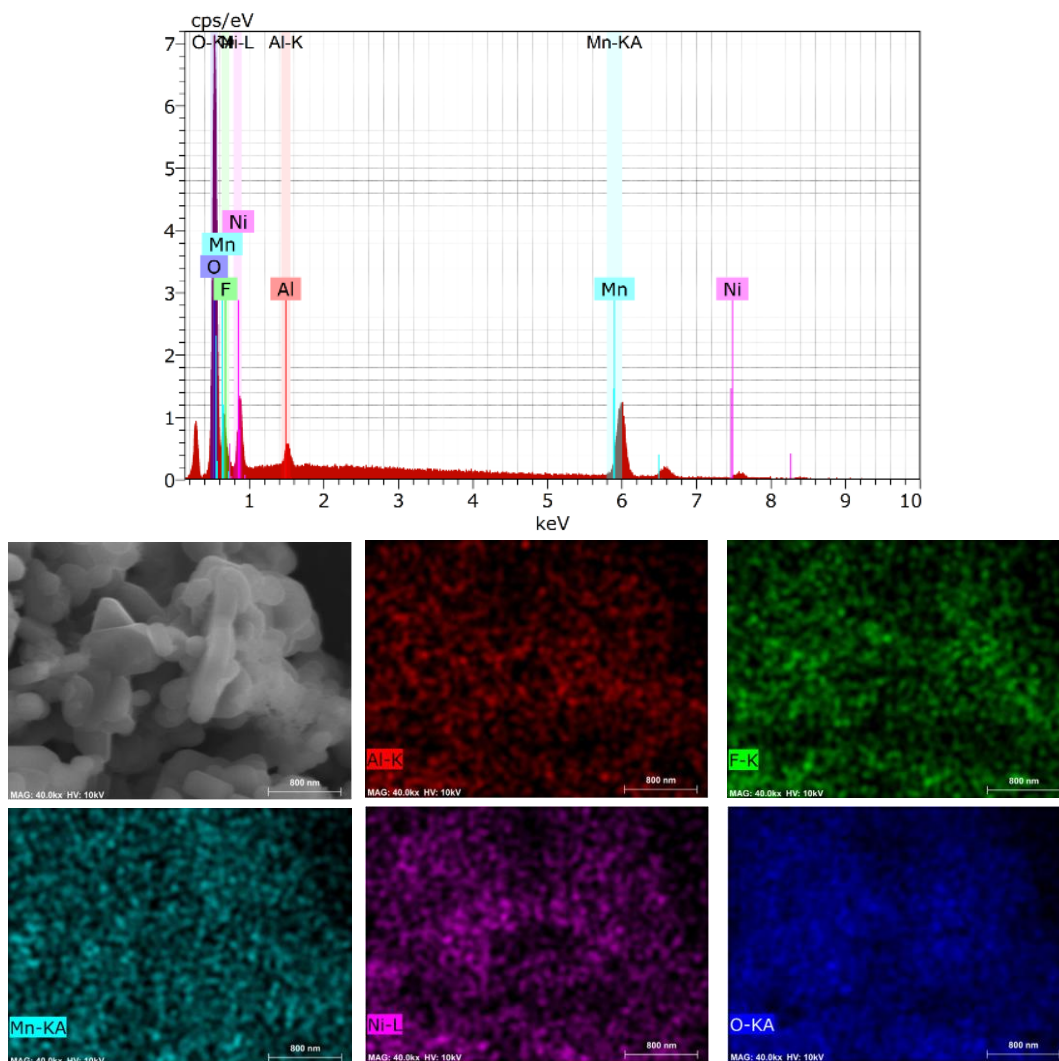
Figure 31. SEM-EDS analysis and mapping of 3wt% AlF_3-coated LMR samples.
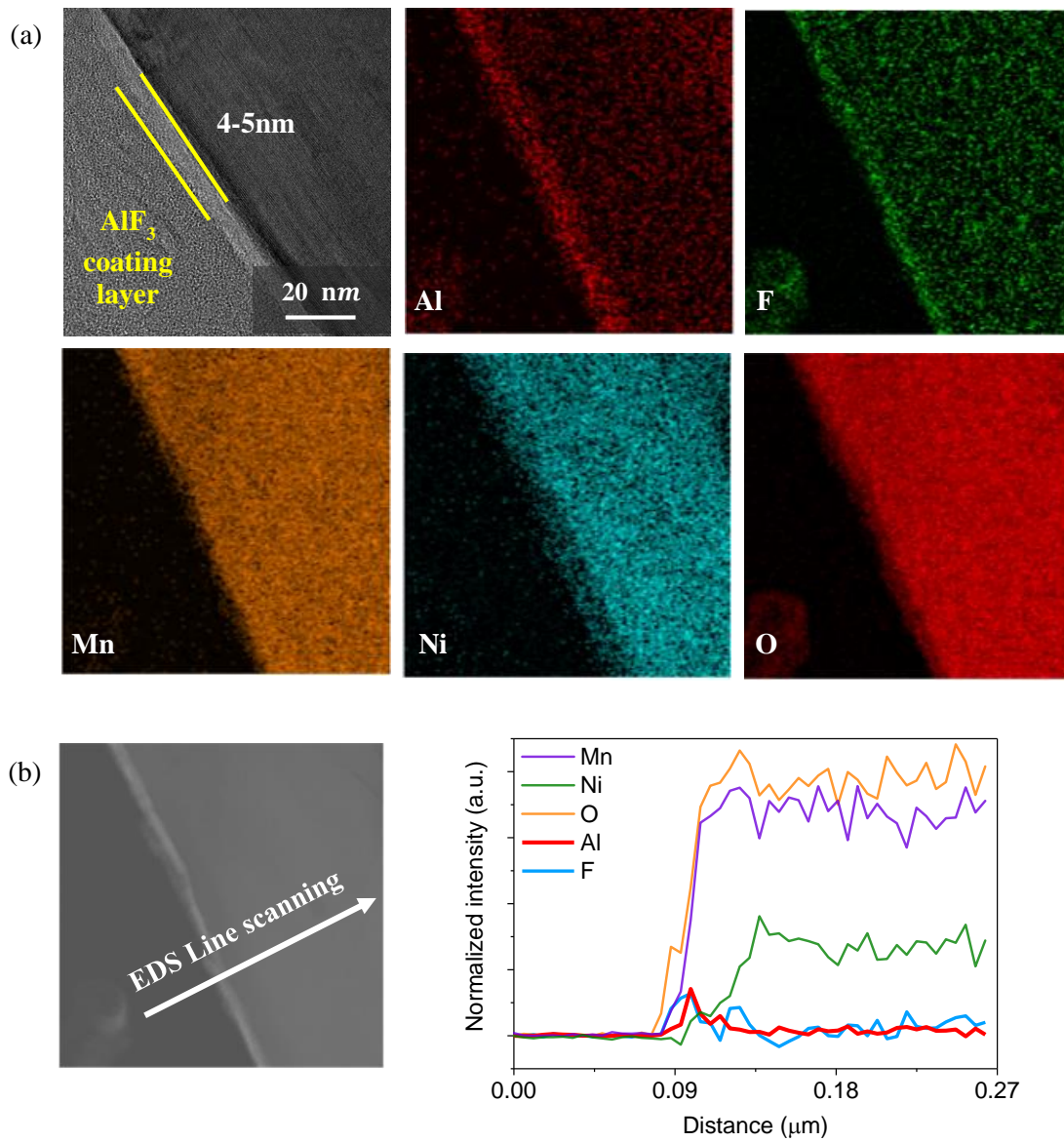
Figure 32. (a) High-resolution TEM image showing the AlF$_3$ coating layer on LMR samples and TEM-EDS mapping. (b) TEM-EDS line scanning of 3wt% AlF$_3$-coated LMR samples.

Figure 33 shows the voltage profiles of the first cycle for the uncoated and 1, 3, 5wt% AlF$_3$-coated samples. As summarized in **Table 5**, the plateau around 4.4V decreases and the initial charge capacity decreases when the weight fraction of AlF$_3$ coating increases. It implies that the I.C.E gradually enhances as the weight fraction of AlF$_3$ coating increases. When comparing with the uncoated sample, I.C.E of the 5wt% AlF$_3$-coated sample is increased by 16.8% from 72.8% to 89.6%. The irreversible capacity was also greatly reduced from 94mAh/g to 29.8mAh/g.
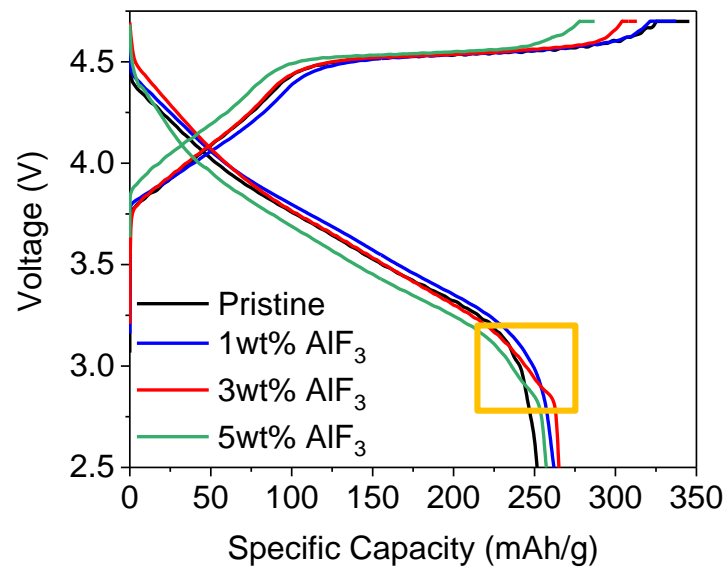
Figure 33. Voltage profiles of pristine and 1,3,5wt% AlF$_3$-coated samples in the range of 2.5-4.7V at 0.2C.

Samples	1st Charge capacity (mAh/g)	1st Discharge capacity (mAh/g)	I.C.E (%)
Pristine	345.6	251.6	72.8
1wt% AlF$_3$	337.5	262.0	77.6
3wt% AlF$_3$	313.2	265.1	84.6
5wt% AlF$_3$	287.1	257.3	89.6

Table 5. Initial charge/discharge capacity and Coulombic efficiency of pristine and 1, 3, 5wt% AlF$_3$-coated MN7525 samples.

The more important thing to note is that a short voltage plateau around 2.8V is only formed in the 3wt% and 5wt% AlF$_3$-coated samples. From the dQ/dV plot for the first cycle, it is observed that the extra capacity is newly achieved around 2.8V when the weight fraction of AlF$_3$ is 3wt% or higher (**Figure 34**). This phenomenon implies that the spinel phase is formed on the 3wt% and 5wt% AlF$_3$-coated samples obviously during the first cycle. It indicates that the Li$_2$MnO$_3$ phase is electrochemically activated rapidly, and thus, initial discharge capacity increases. However, the initial discharge capacity is the highest in the 3wt% AlF$_3$-coated sample, and for 5wt%, the capacity is slightly decreased. Also, it seems that the overpotential in the 5wt% AlF$_3$-coated sample is significantly high. Therefore, we selected 3wt% AlF$_3$-coated sample as an optimal product and conducted electrochemical and structural in-depth analysis with this material. A schematic diagram of the AlF$_3$-coated particle after the first cycle is illustrated in **Figure 35**. During the first cycle, chemical activation of Li$_2$MnO$_3$ phase occurs from the surface of the AlF$_3$-coated particles. The chemically activated layer is formed under the AlF$_3$ coating layer. The MO$_2$ (M=Mn, Ni) phase generated in the first charge process is lithiated in the subsequent discharge process, thereby forming a defect-spinel structure of LiMn$_2$O$_4$ and LiMn$_3$O$_4$ phases.
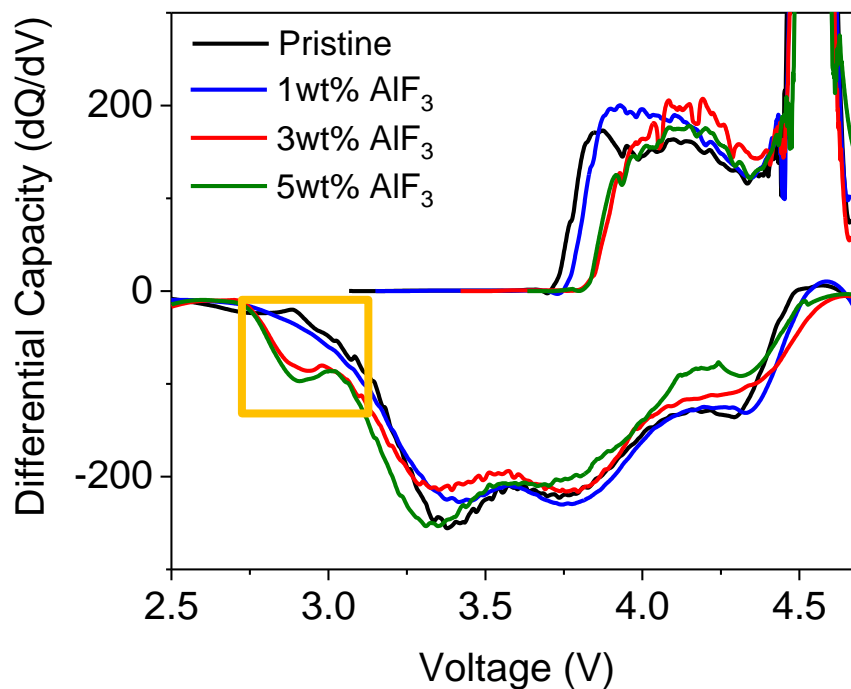
Figure 34. dQ/dV profiles at 0.2C derived from the initial cycles.
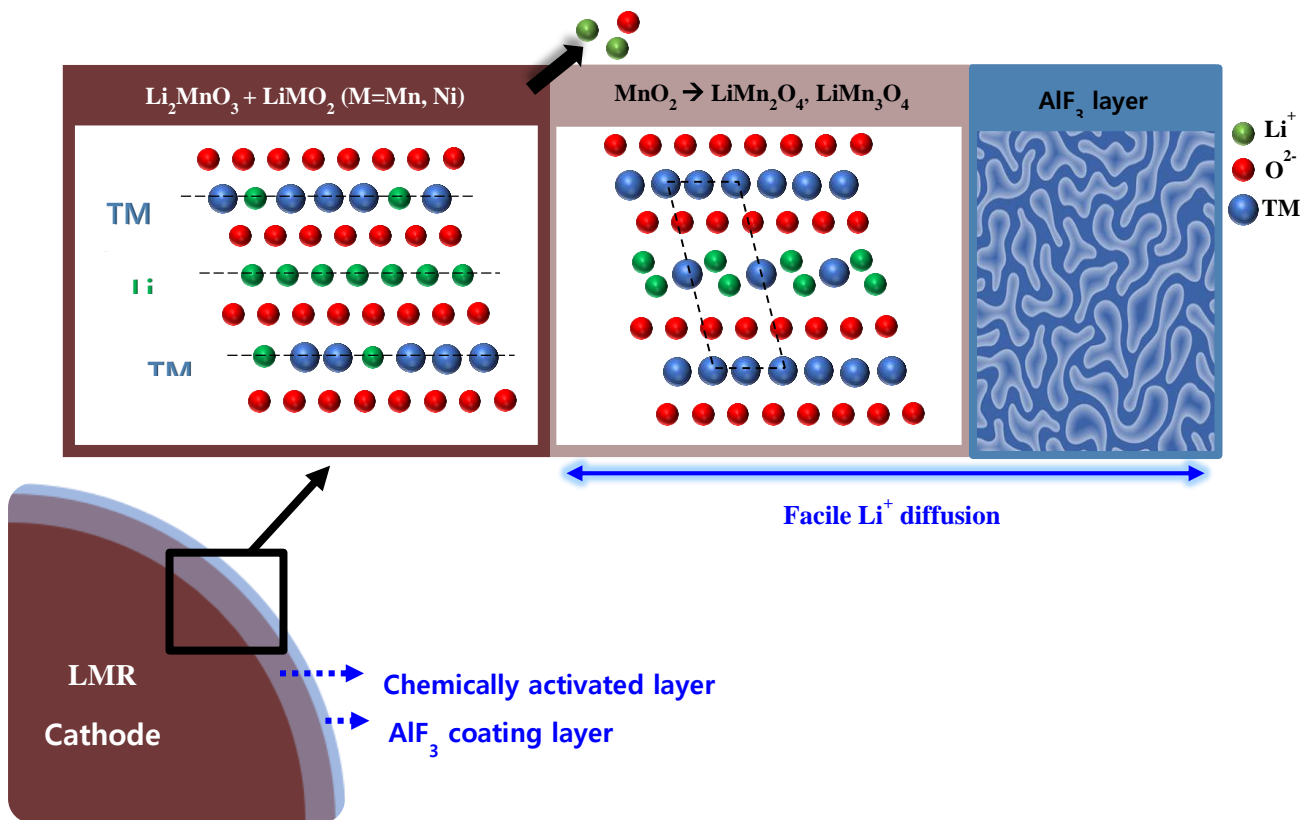
Figure 35. Schematic illustrations of the structure of AlF$_3$-coated LMRs after the first cycle.

Figure 36 shows the discharge capacity and capacity retention of the pristine and 3wt% AlF$_3$-coated samples from the first two formation cycles at 0.2C to the 42nd cycle at 1C-rate. For the second formation cycle, the discharge capacity of the pristine sample is 244.6mAh/g, and that of the 3wt% AlF$_3$-coated sample is 252.4mAh/g. When the current applied is increased to 1C, the discharge capacity is decreased to 188.2mAh/g and 209.7mAh/g, respectively. The AlF$_3$-coated sample can retain the discharge capacity more than the uncoated sample about 13.7mAh/g. From the top graph of **Figure 36**, it seems that the capacity retention of the uncoated sample is slightly higher than the AlF$_3$-coated sample. Considering the discharge capacity of the formation cycle, however, the AlF$_3$-coated sample shows higher capacity retention. Also, the bottom graph of **Figure 36** demonstrates that the AlF$_3$-coated sample achieves higher discharge capacity constantly during 40 cycles.
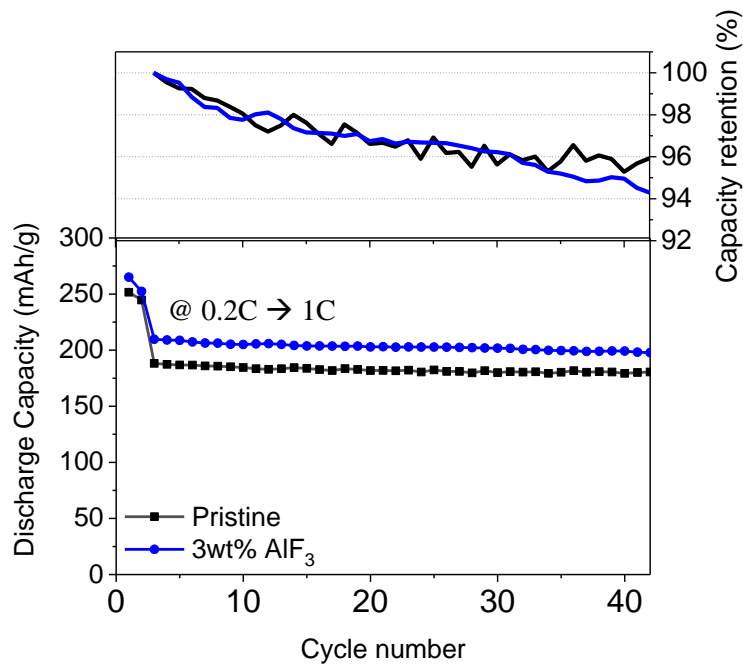
Figure 36. The change of discharge capacity and the retention of pristine and 3wt% AlF_3-coated sample as a function of the number of cycles.

Figure 37 shows the comparison of the rate capabilities of the 3wt% AlF_3-coated sample and the uncoated sample. As the C-rate is increased, the discharge capacity of the uncoated sample is much more greatly reduced. As a result, the difference of capacity between two samples is getting bigger as the current applied increases. In particular, it is observed that the capacity retention of the uncoated sample is sharply decreased showing a slope when the C-rate is increased to 3C. This result suggests that the AlF_3 coating layer acts as a buffer layer, enabling facile lithium ion diffusion.
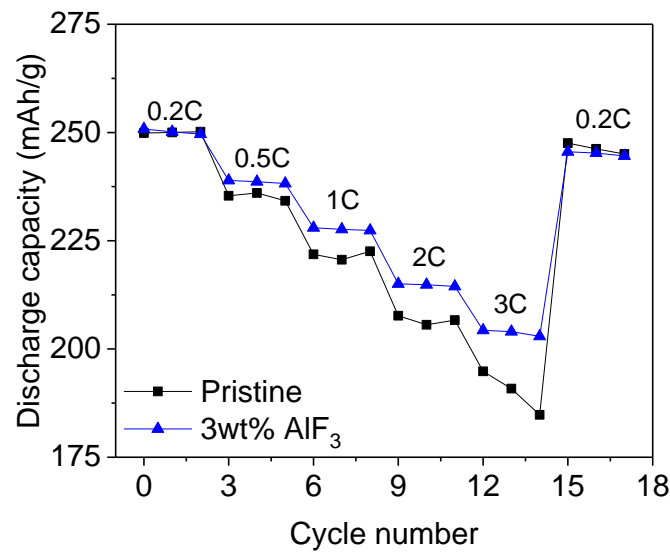
Figure 37. Rate capabilities of the pristine and 3wt% AlF$_3$-coated MN7525 in the voltage range 2.5-4.6V.

In order to find out the origin of increase in rate capabilities, analysis of electrochemical impedance spectra (EIS) is conducted for the uncoated samples and 3wt% AlF$_3$-coated samples. **Figures 38** shows Nyquist plots from EIS, which compare the resistance of each sample before and after cycling. Intercept at real axis represents the overall solution resistance (R_{sol}) of the cell, a semicircle in the high-frequency region is the resistance caused by a SEI layer (R_{SEI}), and a semicircle in intermediate-frequency indicates the charge transfer resistance (R_{ct}) at the interface. Each resistance parameter for the Nyquist plots is summarized in **Table 6**. Both samples have similar R_{sol} values before and after the cycle, and they have increased by 0.4Ω. However, R_{SEI} and R_{ct} show different patterns. The R_{SEI} of the uncoated sample before and after the cycle is 3.0Ω and 4.8Ω, respectively, which has increased by 1.8Ω. On the other hand, the R_{SEI} of the AlF$_3$-coated sample just has increased by 1.2Ω from 2.5Ω to 3.7Ω. It can be evidence that the AlF$_3$ coating layer plays a role in preventing the formation of a thick SEI layer. It acts as a buffer layer by preventing direct contact with liquid electrolyte and cathode material, thereby the side reactions are mitigated.

The biggest difference between two samples is represented in R_{ct} values. The gap of R_{ct} value between two samples is very large. Even before the cycle, the difference is evident. The resistance value is 6.6Ω for the uncoated sample, and 5.2Ω for the AlF_3-coated sample. The gap between two is 1.4Ω. This result implies that AlF_3 coating has the greatest influence on improving the kinetics related to charge transfer reaction. The facile lithium ion diffusion with the reduction of charge transfer resistance would be ascribed to main two reasons. The first reason is that the outermost AlF_3 layer has an amorphous structure, and the second reason is that the spinel phase is quickly generated on the surface of the particles in advance during the formation cycles. The interphase with this unique structure makes the charge transfer between the particles more easily. It emphasizes the importance of an effective activation process of Li_2MnO_3 phase, which has high crystallinity. After cycling, the difference between two samples becomes even greater to 2.2Ω. When comparing the increase in R_{ct}, 1.6Ω for uncoated sample and 0.8Ω for the AlF_3-coated sample is increased. It shows the role of AlF_3 layer as a buffer layer once again. By preventing the occurrence of microcracks and the disconnection between the active materials, AlF_3 buffer layer plays a critical role in decreasing the charge transfer resistance. It is highly related to the resistance by SEI layer above.

The chemical effect of AlF_3 coating layer can be also demonstrated through the profile of Warburg impedance caused by mass transport. It is observable in the low-frequency region with a shape of line. If the Warburg impedance shows a straight line with an angle of 45°, it indicates CPE (Constant Phase Element), where the state of boundary is a semi-infinite diffusion layer. If a semi-circle is shown instead of a straight line, it is FLW (Finite Length Warburg), which has the boundary with finite diffusion length. In the case of the uncoated sample, the semi-circle profile is shown in the Warburg impedance region, and its slopes and diameters are high. The 3wt% AlF_3-coated sample also shows a semi-circle profile in higher frequency, but its size and slope are much smaller than that of the uncoated sample. The bigger difference between two samples can be found in a lower frequency region. The profile of Warburg impedance for 3wt% AlF_3-coated sample is changed into a shape of a straight line. It means that coated sample clearly has a semi-infinite diffusion layer and finite diffusion layer at the same time. It indicates that a new layer is formed on the surface of the particles. Not only AlF_3 coating layer is formed at the interface, but also the spinel structure, which can provide a three-dimensional network for diffusing lithium ions, is generated in advance through the effective electrochemical activation at the first cycle. As mentioned in the previous paragraph, it verifies that the AlF_3 coating can facilitate the lithium ion diffusion. It is also corresponding to the results of electrochemical evaluation and rate capability test above.

These results prove two functions of AlF$_3$ coating. At first, the AlF$_3$ layer at the outermost surface stabilizes the interface by preventing the formation of a thick SEI layer during cycles. Second, with the spinel structure generated below the coating layer, facile lithium ion diffusion can be possible. As a result, interfacial stability as well as rate capability can be highly enhanced.
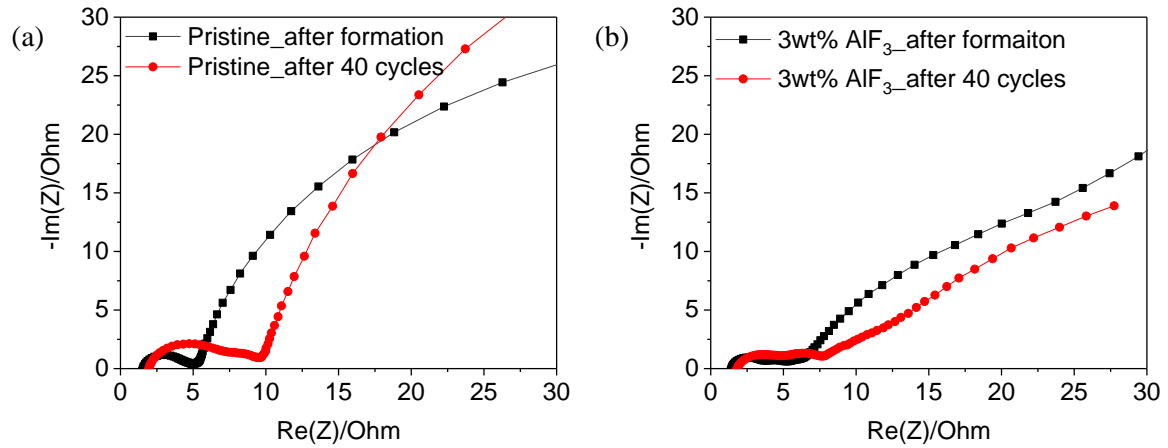
Figure 38. Nyquist plots from electrochemical impedance spectroscopy (EIS) of (a) pristine and (b) 3wt% AlF$_3$-coated samples comparing the impedance before and after cycling.

	Pristine		3wt% AlF$_3$-coated	
	After formation	After 40 cycles	After formation	After 40 cycles
R_{sol} (Ω)	1.5	1.9	1.4	1.8
R_{SEI} (Ω)	3.0	4.8	2.5	3.7
R_{ct} (Ω)	6.6	8.2	5.2	6.0

Table 6. Impedance parameters obtained from electrochemical impedance spectroscopy (EIS).

From now on, we verified the above-mentioned phenomena in detail by observing the microstructures of each sample with high resolution scanning transmission electron microscopy (HR-STEM). **Figure 39** and **Figure 40** show the HR-STEM images of uncoated and 3wt% AlF_3-coated sample after 40 cycles, respectively. In **Figure 39a**, a high-angle annular dark-field (HAADF)-STEM image of uncoated sample, transition metal exists in lithium ion layer on the surface side. It means that cation mixing occurs at the interface. Through the results of FFT analysis and their signal profiles, it is clearly observed that the phase transition to rock-salt phase has occurred in the surface region even though the layered structure is well maintained in the bulk (**Figure 39b, 39c**). Generally, the distance between transition metal layers is approximately 0.47nm along the [100] monoclinic direction. The signal profiles at the bulk region indicate that it has a layered structure with a spacing of 0.48nm. On the other hand, new peaks with low intensity have appeared near the surface, and the spacing between the nearest peaks is decreased to 0.25nm. It implies that a new layer is formed between the transition metal layers, and further phase transformation happens.

In a bright field (BF)-STEM image of the 3wt% AlF_3-coated sample (**Figure 40a**), the layered structure is well maintained in the bulk site in common with the uncoated sample. The obvious difference is the structural changes at the surface. Unlike the uncoated sample, which shows a phase transition to rock-salt phase, the AlF_3-coated sample has spinel structure. It is demonstrated through FFT analysis and its signal profiles represented in **Figure 40b** and **40c**. FFT patterns confirm that the structure of AlF_3-coated sample near the surface is partially mixed with the spinel phase. The signal patterns show that the distance between transition metal layers is about 0.5nm. Although the spacing is slightly larger than the layered structure, the intensities of the peaks are almost the same. It indicates that severe phase transformation to the rock-salt structure did not happen. In general, the phase transition of the LMR occurs by oxygen deficiency. Depending on that degree, the layered structure becomes a rock-salt structure through a spinel structure. That is to say, the reason why the degree of phase transformation occurs differently between the two samples is the different degree of oxygen deficiency. This result supports that the AlF_3 layer contributes to preventing surface oxygen release during the cycle, leading to a low degree of phase transition.
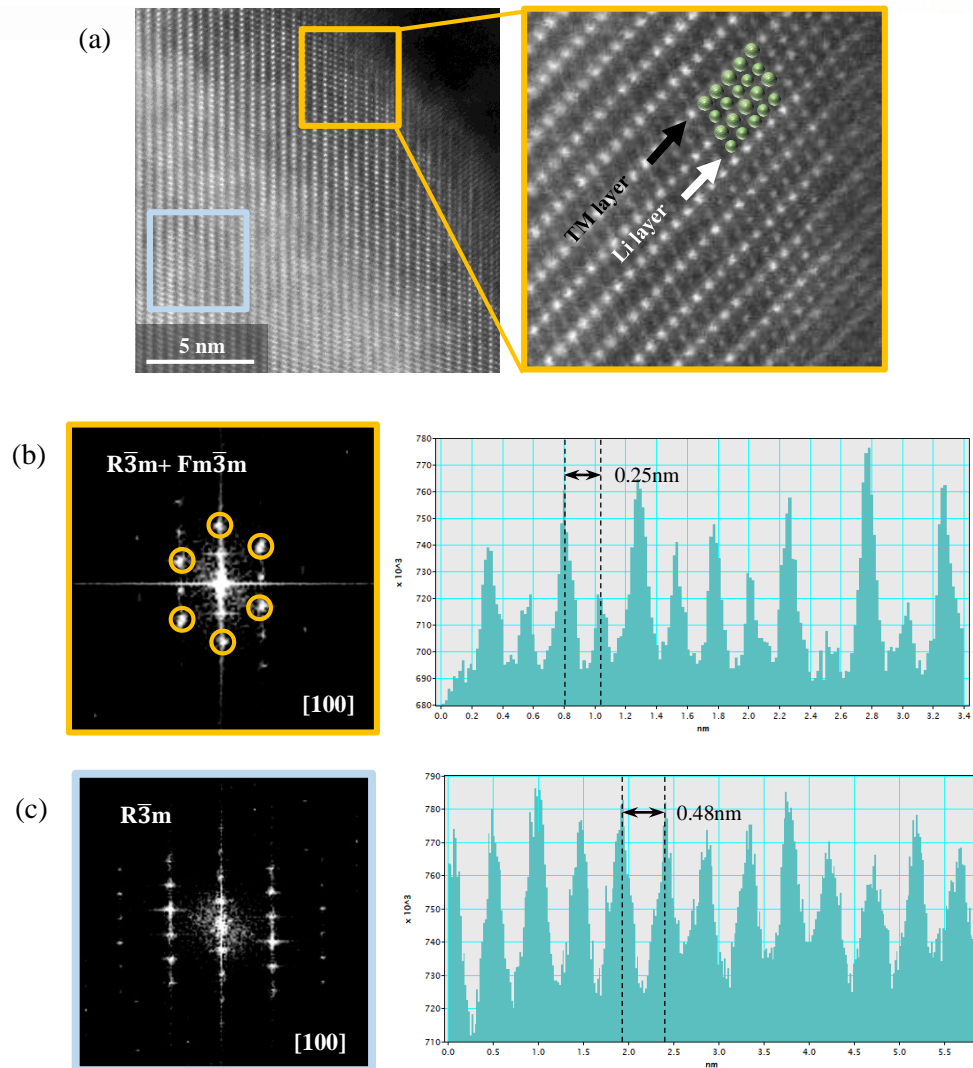
Figure 39. Microstructure of pristine samples after cycling. (a) A HAADF-STEM image of pristine sample at discharge states after cycling and higher magnification image showing its surface. Fast Fourier transform patterns and signal profiles of (b) surface site and (c) bulk site of pristine sample.
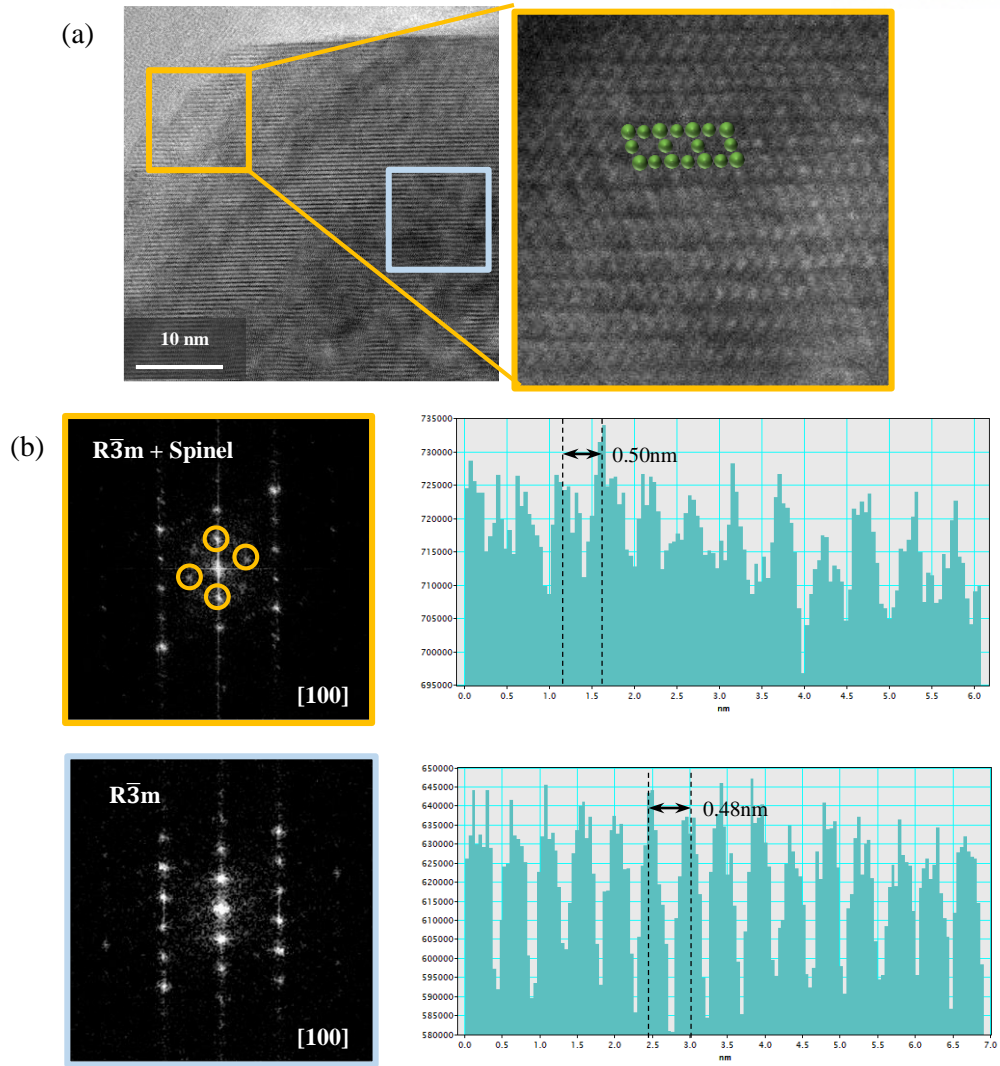
Figure 40. Microstructure of 3wt% AlF$_3$-coated samples after cycling. (a) A BF-STEM image of 3wt% AlF$_3$-coated samples at discharge states after cycling. Fast Fourier transform patterns signal profiles of (b) surface site and (c) bulk site of AlF$_3$-coated sample.

The dQ/dV plots before and after 40 cycles are compared for the uncoated and AlF$_3$-coated samples in **Figure 41**, respectively. It can be related to the result of STEM analysis. During a discharge process, the peak at over 3.6V is generated by a redox reaction of Ni$^{2+/4+}$, and the peak near 3.3V is generated by a reduction reaction of MnO$_2$ phase. For the second cycle, AlF$_3$-coated sample shows slightly lower peak intensity near 3.3V than uncoated sample, and a small new peak is formed around 2.8V. This new peak can be also observed in the uncoated sample, but tis degree is much lower than the AlF$_3$-coated sample. This is because the chemical activation of Li$_2$MnO$_3$ phase has already progressed during the coating process. After 40 cycles, the 3.3V peak intensities of the uncoated and AlF$_3$-coated samples are decreased to almost the same level. Considering the peak intensity in the second cycle, it has decreased even less dramatically in the AlF$_3$-coated sample. Instead, the peak intensity around 2.8V increases. These phenomena can be evidence that the phase transformation to the spinel phase occurs greatly in the AlF$_3$-coated sample for the first cycle, and it continuously takes place during the cycles.
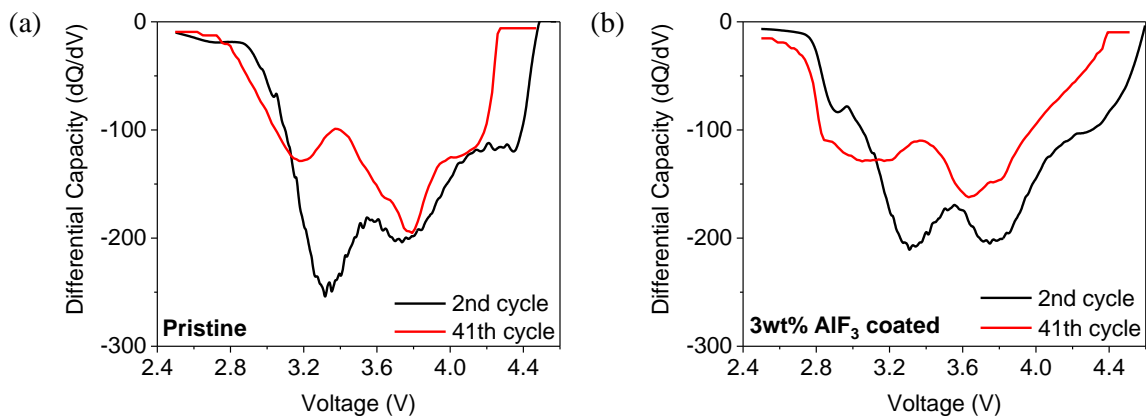
Figure 41. dQ/dV plots of (a) uncoated and (b) 3wt% AlF$_3$-coated samples comparing the 2nd cycle at 0.2C and the 41st cycle at 1C.

TEM-EELS analysis was also conducted in order to correlate the structural change with valence state of each element. **Figure 42** shows the comparison of the O-k edge of uncoated and AlF₃-coated samples before and after cycling at the different regions. There are two differences between the samples at each region. First, in the bulk region, the peak intensity of the uncoated sample has decreased remarkably, whereas that of the AlF₃-coated sample is maintained at almost the same level. Second, in the surface area, the peak intensity of the uncoated sample is significantly reduced even before cycling, and it is further getting lower after 40 cycles. It means the oxygen release has occurred on the surface rapidly from the first cycle. On the other hand, the AlF₃-coated sample shows different tendency. The peak intensity before cycling is very similar to the bulk. As the charge/discharge is repeated, however, the peak has almost disappeared. This result is closely related to the change in the valence state of Mn, thus it will be discussed with the EELS analysis of Mn in next paragraph.
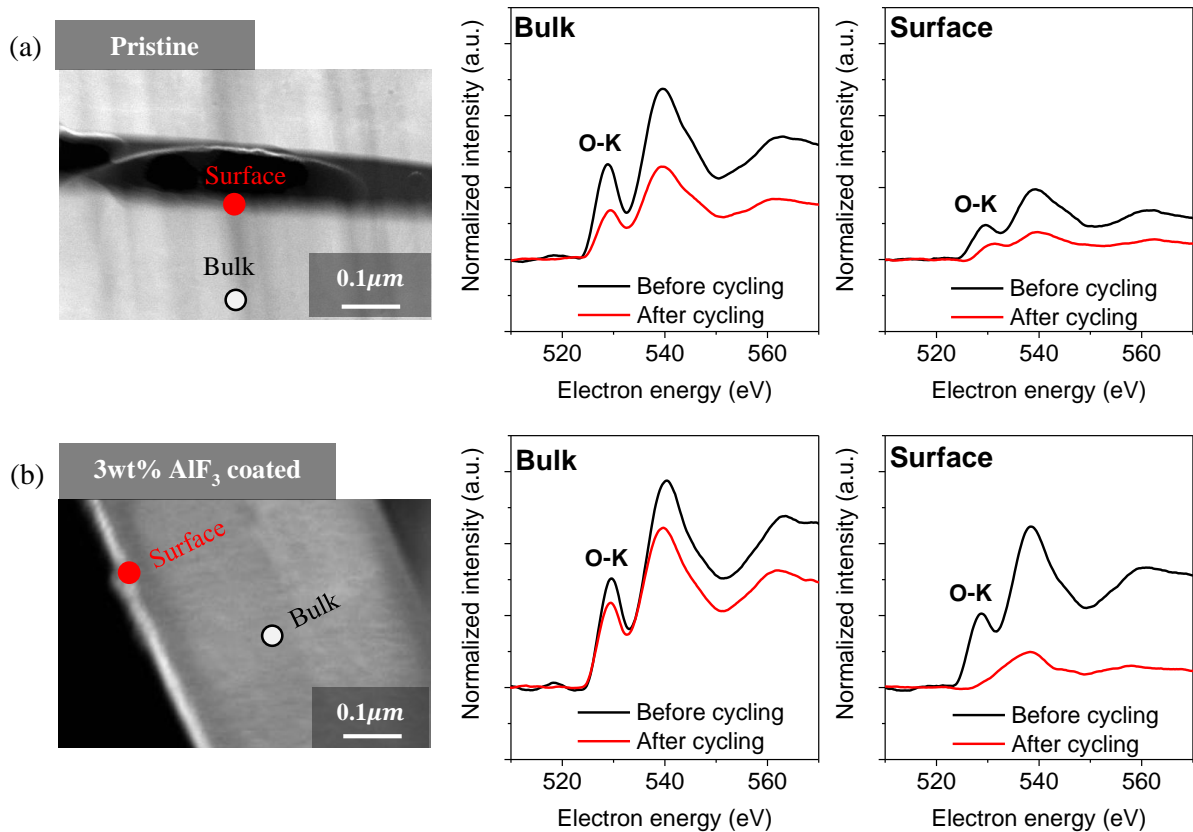
Figure 42. Electron energy loss spectroscopy (EELS) spectra for O-k edge of (a) uncoated and (b) 3wt% AlF₃-coated samples comparing pristine states and discharge (2.0V) states after 40 cycles.

Figure 43 shows the result of EELS spectra for Mn-L edge peak. Both changes of peak intensities in bulk and surface have a similar pattern to that of the O-k edge peak. The important point to note is the valence state of Mn in the AlF$_3$-coated sample near the surface. The Mn-L$_3$ peak and Mn-L$_2$ peak are slightly tilted to the right in all other states, indicating the valence state of Mn is 3+/4+. On the contrary, when observing the peaks of the Mn-L edge on the surface of the AlF$_3$-coated sample, the valence state of Mn has been 3+ after formation cycles. This is because the chemical activation of Li$_2$MnO$_3$ phase has progressed already, generating LiMn$_2$O$_4$ and LiMn$_3$O$_4$ phase at the interface. As the cycle is repeated, the Mn-L peaks are more tilted to the left. It means that Mn is reduced to 2+ to some degree. Due to the charge compensation by the oxygen release at the surface, LiMn$_2$O$_4$ and LiMn$_3$O$_4$ phases with spinel structure are generated more and more from MnO$_2$ and Mn$_3$O$_4$ phases during the discharge process. As a result, the proportion of Mn^{2+} is increased. It is closely associated with the aforementioned large reduction in the O-k edge peak of the AlF$_3$-coated sample at the surface.

Additionally, the changes in Ni-L edge also are represented in **Figure 44**. For Ni-L edge, both the uncoated sample and the AlF$_3$-coated sample have maintained the peak position well after the cycle. However, in the case of an uncoated sample, the peak intensity under all conditions is slightly lower than that of the AlF$_3$-coated sample. Especially at the surface, the intensity is so low that it is unclear to observe the peak regardless of before and after cycling. It can be inferred that AlF$_3$ layer can also reduce the nickel dissolution from the surface. **Figure 45** shows the change of L$_3$/L$_2$ ratio obtained from EELS. Because the cathodes are fully lithiated in both pristine state and discharged state, L$_3$/L$_2$ ratio should be constant. If it has changed during cycling, it would indicate that the cathode undergoes irreversible phase transition. For the Mn L-edge, L$_3$/L$_2$ ratio has changed little at the bulk. At the surface, however, it has changed a lot. The degree of change for the AlF$_3$-coated sample is even larger than the uncoated sample. It is corresponding to the previous analyses, indicating the formation of spinel phase at the interface in larger quantities. In the case of Ni L-edge, the degree of change in the L$_3$/L$_2$ ratio decreases significantly in the AlF$_3$-coated sample at both bulk and surface regions. It means that irreversible change has occurred less in the AlF$_3$-coated sample. That is to say, it can also be evidence that coating layer prevents nickel dissolution and cation mixing.
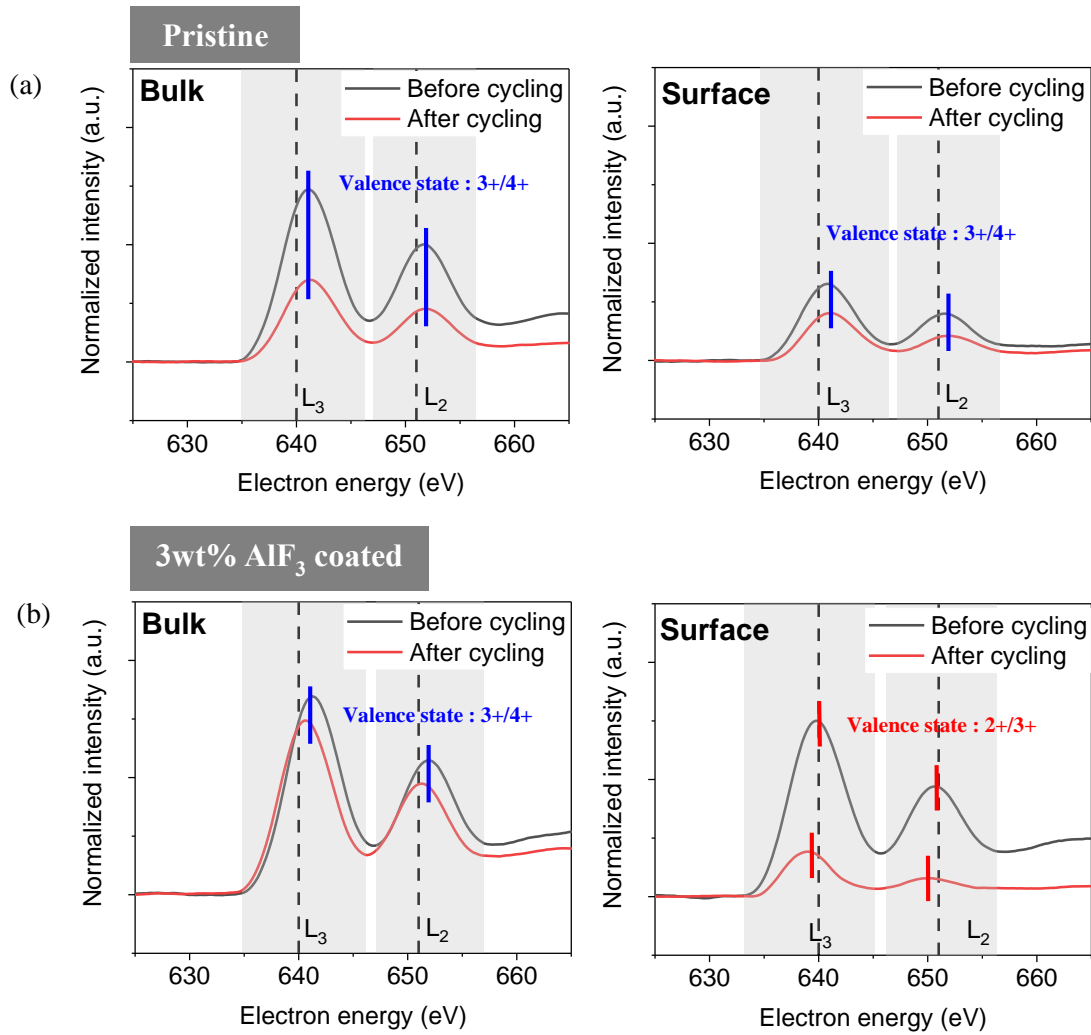
Figure 43. Electron energy loss spectroscopy (EELS) spectra for Mn-L of (a) uncoated and (b) 3wt% AlF$_3$-coated samples comparing pristine states and discharge (2.0V) states after 40 cycles.
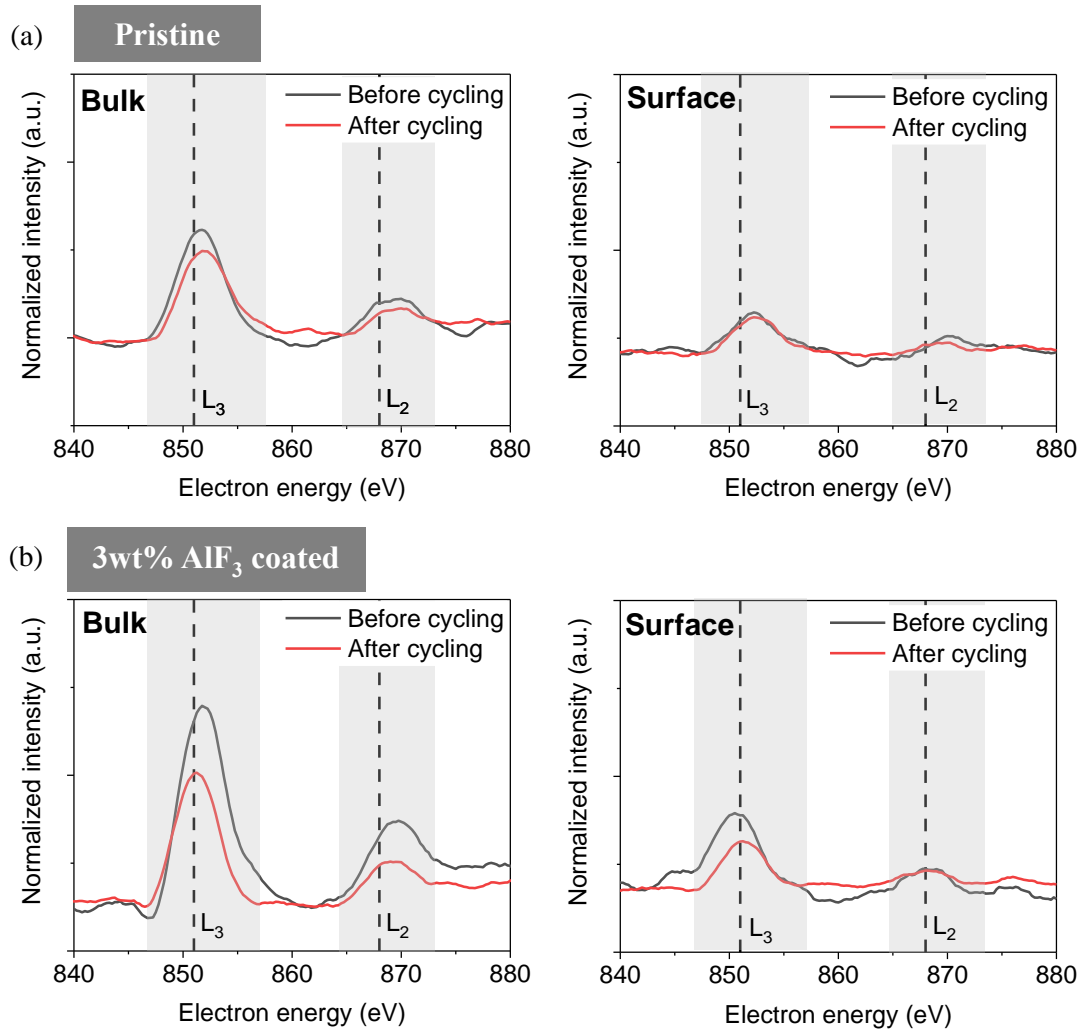
Figure 44. Electron energy loss spectroscopy (EELS) spectra for Ni-L edge of (a) uncoated and (b) 3wt% AlF_3-coated samples comparing pristine states and discharge (2.0V) states after 40 cycles.
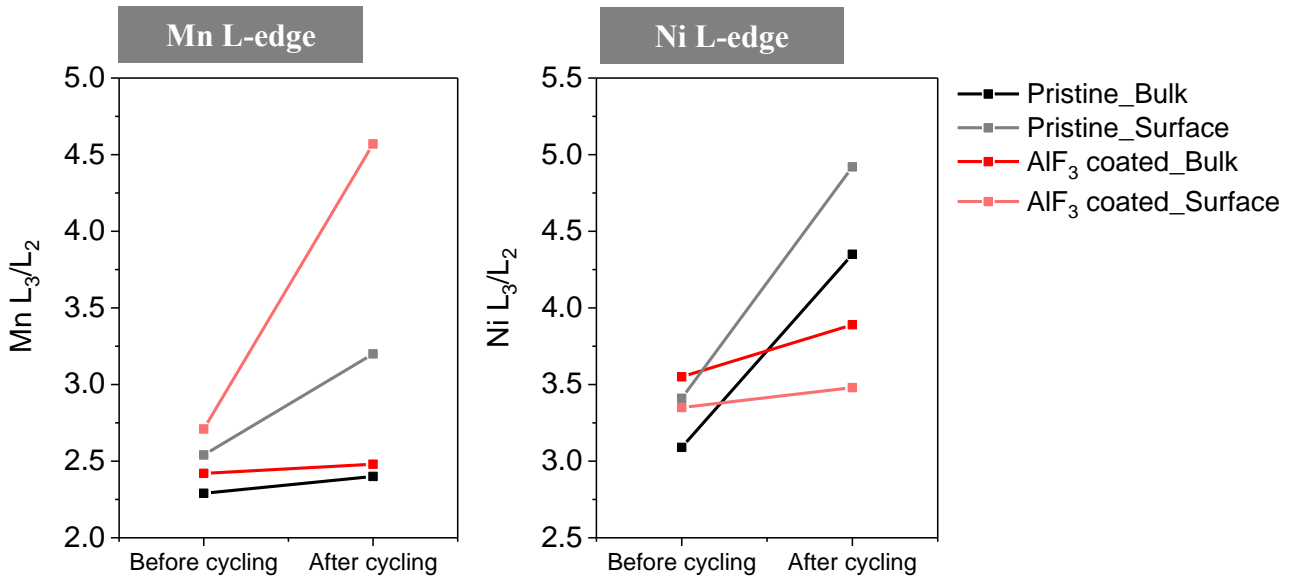
Figure 45. L_3/L_2 ratios obtained from EELS of uncoated and 3wt% AlF_3-coated samples comparing pristine states and discharge (2.0V) states after 40 cycles.

From the analysis of all TEM and dQ/dV data, it is confirmed that the AlF_3 coating layer generates the layer of spinel structure on the surface rapidly. Even though it seems that large phase transformation has occurred, this reaction arises only on the surface and it acts as a protective layer of LMR materials. It prevents the oxygen evolution inside the particles, thereby inhibiting the phase transition to rock-salt phase as well as transition metal dissolution.

IV. Conclusion

This work has introduced a hybrid strategy that combines morphology control and surface coating to LMRs in order to resolve both problems of low volumetrical energy density and high irreversibility. We have shown that controlling the morphology of primary particle with flake-type shape improves cycle stability and rate capabilities. Since the surface area that directly contacts with electrolyte decreases, the side reactions are relieved. As a result, the formation of thick SEI, the occurrence of microcracks and phase transition are greatly reduced. In addition, as the number of grain boundaries where lithium ions and electrons move during the lithiation/delithiation process decreases, the overpotential regarding the charge transfer reduces. This property eventually enhances the rate capability. Due to the trade-off relationship between the particle size and reversibility, however, LMRs with flake-type shape show high irreversibility inevitably. To improve it, surface coating with AlF_3 was introduced as the second method. We have demonstrated that surface modification with AlF_3 coating has two functions as follows; 1) It stabilizes the interface between electrode and electrolyte, leading to decrease of phase transition to rock-salt phase by preventing oxygen evolution at the surface. 2) It helps to activate the Li_2MnO_3 phase in the first cycle rapidly, thereby phase transition to spinel structure occurs at the interface after the formation cycles. With the amorphous AlF_3 coating layer at the outermost region and the internal 3D diffusion pathway of spinel phase, lithium ion diffusion becomes more facile and extra capacity around 2.8V is newly achieved. Consequently, the poor kinetics of LMRs, such as low I.C.E, severe voltage decay and low rate capabilities, can be highly improved at the same time. With these properties, LMRs can achieve high volumetric energy density and maintain it as the cycle repeats. We believe that this work with the combined method can contribute to the development of practical applicable LMRs.

References

1. Grimaud, A., et al., Anionic redox processes for electrochemical devices. Nature Materials, 2016. 15(2): p. 121-126.

2. Boulineau, A., et al., First Evidence of Manganese–Nickel Segregation and Densification upon Cycling in Li-Rich Layered Oxides for Lithium Batteries. Nano Letters, 2013. 13(8): p. 3857-3863.

3. Ding, Y., et al., Automotive Li-Ion Batteries: Current Status and Future Perspectives. Electrochemical Energy Reviews, 2019. 2(1): p. 1-28.

4. Zheng, J., et al., Functioning Mechanism of AlF_3 Coating on the Li- and Mn-Rich Cathode Materials. Chemistry of Materials, 2014. 26(22): p. 6320-6327.

5. Rozier, P. and J.M. Tarascon, Review—Li-Rich Layered Oxide Cathodes for Next-Generation Li-Ion Batteries: Chances and Challenges. Journal of The Electrochemical Society, 2015. 162(14): p. A2490-A2499.

6. Zheng, J., et al., Structural and Chemical Evolution of Li- and Mn-Rich Layered Cathode Material. Chemistry of Materials, 2015. 27(4): p. 1381-1390.

7. Thackeray, M.M., et al., Li_2MnO_3-stabilized $LiMO_2$ (M = Mn, Ni, Co) electrodes for lithium-ion batteries. Journal of Materials Chemistry, 2007. 17(30): p. 3112-3125.

8. Oh, P., et al., Superior Long-Term Energy Retention and Volumetric Energy Density for Li-Rich Cathode Materials. Nano Letters, 2014. 14(10): p. 5965-5972.

9. Hong, J., et al., Review—Lithium-Excess Layered Cathodes for Lithium Rechargeable Batteries. Journal of The Electrochemical Society, 2015. 162(14): p. A2447-A2467.

10. Hong, J., et al., Critical Role of Oxygen Evolved from Layered Li–Excess Metal Oxides in Lithium Rechargeable Batteries. Chemistry of Materials, 2012. 24(14): p. 2692-2697.

11. Han, J.-G., et al., Unsymmetrical fluorinated malonatoborate as an amphoteric additive for high-energy-density lithium-ion batteries. Energy & Environmental Science, 2018. 11(6): p. 1552-1562.

12. Zheng, J., et al., Li- and Mn-Rich Cathode Materials: Challenges to Commercialization. Advanced Energy Materials, 2017. 7(6): p. 1601284.

13. Shimoda, K., et al., Direct observation of layered-to-spinel phase transformation in Li_2MnO_3 and the spinel structure stabilised after the activation process. Journal of Materials Chemistry A, 2017. 5(14): p. 6695-6707.

14. Hu, E., et al., Evolution of redox couples in Li- and Mn-rich cathode materials and mitigation of voltage fade by reducing oxygen release. Nature Energy, 2018. 3(8): p. 690-698.

15. Singer, A., et al., Nucleation of dislocations and their dynamics in layered oxide cathode materials during battery charging. Nature Energy, 2018. 3(8): p. 641-647.

16. Cho, J., S. Jeong, and Y. Kim, Commercial and research battery technologies for electrical energy storage applications. Progress in Energy and Combustion Science, 2015. 48: p. 84-101.

17. Choi, J.W. and D. Aurbach, Promise and reality of post-lithium-ion batteries with high energy densities. Nature Reviews Materials, 2016. 1(4): p. 16013.

18. Tarascon, J.M. and M. Armand, Issues and Challenges Facing Rechargeable Lithium Batteries. Nature, 2001. 414: p. 359-67.

19. Li, W., E.M. Erickson, and A. Manthiram, High-nickel layered oxide cathodes for lithium-based automotive batteries. Nature Energy, 2020. 5(1): p. 26-34.

20. Pan, H., et al., Li- and Mn-rich layered oxide cathode materials for lithium-ion batteries: a review from fundamentals to research progress and applications. Molecular Systems Design & Engineering, 2018. 3(5): p. 748-803.

21. Li, X., et al., Direct Visualization of the Reversible O2−/O− Redox Process in Li-Rich Cathode Materials. Advanced Materials, 2018. 30(14): p. 1705197.

22. Johnson, C.S., et al., The significance of the Li2MnO3 component in 'composite' xLi2MnO3·(1−x)LiMn0.5Ni0.5O2 electrodes. Electrochemistry Communications, 2004. 6(10): p. 1085-1091.

23. Carroll, K.J., et al., Probing the electrode/electrolyte interface in the lithium excess layered oxide Li1.2Ni0.2Mn0.6O2. Physical Chemistry Chemical Physics, 2013. 15(26): p. 11128-11138.

24. Erickson, E.M., et al., Review—Recent Advances and Remaining Challenges for Lithium Ion Battery Cathodes. Journal of The Electrochemical Society, 2017. 164(1): p. A6341-A6348.

25. Seo, D.-H., et al., The structural and chemical origin of the oxygen redox activity in layered and cation-disordered Li-excess cathode materials. Nature Chemistry, 2016. 8(7): p. 692-697.

26. Luo, K., et al., Anion Redox Chemistry in the Cobalt Free 3d Transition Metal Oxide Intercalation Electrode Li[Li0.2Ni0.2Mn0.6]O2. Journal of the American Chemical Society, 2016. 138(35): p. 11211-11218.

27. Sathiya, M., et al., Reversible anionic redox chemistry in high-capacity layered-oxide electrodes. Nature Materials, 2013. 12(9): p. 827-835.

28. Yu, X., et al., Understanding the Rate Capability of High-Energy-Density Li-Rich Layered Li1.2Ni0.15Co0.1Mn0.55O2 Cathode Materials. Advanced Energy Materials, 2014. 4(5): p. 1300950.

29. Lei, Y., et al., Surface Modification of Li-Rich Mn-Based Layered Oxide Cathodes:

Challenges, Materials, Methods, and Characterization. Advanced Energy Materials, 2020. 10(41): p. 2002506.

30. Hwang, J., et al., Excess-Li Localization Triggers Chemical Irreversibility in Li- and Mn-Rich Layered Oxides. Advanced Materials, 2020. 32(34): p. 2001944.

31. Shen, S., et al., Tuning Electrochemical Properties of Li-Rich Layered Oxide Cathodes by Adjusting Co/Ni Ratios and Mechanism Investigation Using in situ X-ray Diffraction and Online Continuous Flow Differential Electrochemical Mass Spectrometry. ACS Applied Materials & Interfaces, 2018. 10(15): p. 12666-12677.

32. Choi, H., et al., Investigating the particle size effect on the electrochemical performance and degradation of cobalt-free lithium-rich layered oxide Li1.2Ni0.2Mn0.6O2. Electrochimica Acta, 2022. 430: p. 141047.

33. Mao, Y., et al., High-Voltage Charging-Induced Strain, Heterogeneity, and Micro-Cracks in Secondary Particles of a Nickel-Rich Layered Cathode Material. Advanced Functional Materials, 2019. 29(18): p. 1900247.

34. Yan, P., et al., Intragranular cracking as a critical barrier for high-voltage usage of layer-structured cathode for lithium-ion batteries. Nature Communications, 2017. 8(1): p. 14101.

35. House, R.A., et al., First-cycle voltage hysteresis in Li-rich 3d cathodes associated with molecular O2 trapped in the bulk. Nature Energy, 2020. 5(10): p. 777-785.

36. Liu, T., et al., Origin of structural degradation in Li-rich layered oxide cathode. Nature, 2022. 606(7913): p. 305-312.

37. Luo, K., et al., Charge-compensation in 3d-transition-metal-oxide intercalation cathodes through the generation of localized electron holes on oxygen. Nature Chemistry, 2016. 8(7): p. 684-691.

38. Wu, F., et al., Renovating the electrode-electrolyte interphase for layered lithium- & manganese-rich oxides. Energy Storage Materials, 2020. 28: p. 383-392.

39. Fu, F., et al., Structure dependent electrochemical performance of Li-rich layered oxides in lithium-ion batteries. Nano Energy, 2017. 35: p. 370-378.

40. Wang, Q.Y., et al., High capacity double-layer surface modified Li[Li0.2Mn0.54Ni0.13Co0.13]O2 cathode with improved rate capability. Journal of Materials Chemistry, 2009. 19(28): p. 4965-4972.

41. Zou, T., et al., Improvement of the electrochemical performance of Li1.2Ni0.13Co0.13Mn0.54O2 cathode material by Al2O3 surface coating. Journal of Electroanalytical Chemistry, 2020. 859: p. 113845.

42. Sun, S., et al., AlF3 Surface-Coated Li[Li0.2Ni0.17Co0.07Mn0.56]O2 Nanoparticles with Superior Electrochemical Performance for Lithium-Ion Batteries. ChemSusChem, 2015.

8(15): p. 2544-2550.

43. Yuan, W., et al., Surface modification of Li(Li0.17Ni0.2Co0.05Mn0.58)O2 with CeO2 as cathode material for Li-ion batteries. Electrochimica Acta, 2014. 135: p. 199-207.

44. Shi, S.J., et al., Enhanced cycling stability of Li[Li0.2Mn0.54Ni0.13Co0.13]O2 by surface modification of MgO with melting impregnation method. Electrochimica Acta, 2013. 88: p. 671-679.

Acknowledgement

2 년이라는 짧은 석사 생활이었지만 많은 가르침을 주신 조재필 교수님께 감사의 말씀드립니다. 항상 열정적이고 도전적인 모습을 보여주신 교수님! 정말 존경합니다~ 교수님의 제자가 될 수 있어서 너무 영광스럽습니다. 제가 회사에 들어가고 난 후에도 교수님의 모습을 본받아 열정적인 사람이 될 수 있도록 노력하겠습니다. 교수님, 항상 건강하시고 한남더힐로 이사 가시면 저희 쓰리진 꼭 초대해주세요!!

저의 석사학위 논문을 심사 해주신 김영식 교수님, 서동화 교수님께도 정말 감사드립니다. 바쁘신 와중에도 참석해주시고 많은 조언 해주셔서, 더욱 깊이 생각해보고 공부해 볼 수 있는 기회를 가질 수 있었습니다. 감사합니다.

그리고 짧은 기간이었지만 정말 많은 것을 가르쳐주고 알려주고 떠난 공침대장 재성오빠에게도 감사의 말씀드립니다. 떠난 후에 많이 바쁠 텐데도 불구하고, 질문에 항상 잘 답해주고 조언해줘서 정말 너무 감동이었어요. 처음 연구실에 들어왔을 때 많이 챙겨주고 대학원 생활의 즐거움을 일깨워준 형연언니, 재경오빠, 태용오빠, 효명오빠, 그리고 대학원 생활은 함께 못했지만 응원 많이 해준 우영오빠에게도 정말 감사드립니다. 언젠가 다같이 얼굴 볼 수 있는 날이 꼭 오기를 바랍니다. 다음으로 우리 쓰리진! 거대한 연구실을 세 명이서 관리하기 힘들었지만 그래도 우리 서로 도와가면서 잘 버틸 수 있었던 것 같아. 다같이 졸업할 줄 알았는데, 홀로 연구실에 남을 유진이. 남은 박사 생활 파이팅! 김박사님 되도 우리 동기들 잊으면 안돼~ 그리고 대전 이웃주민 된 문진언니. 우리 대전에 가서도 자주 만나서 같이 테니스도 치고 재밌게 놀자구~

다음으로, 항상 나를 믿고 응원해준 우리 엄마 아빠. 너무 고맙고 사랑합니다. 엄마 아빠의 응원과 지지 덕분에 지금까지 잘 버텨왔던 것 같습니다. 앞으로 더 자랑스러운 딸이 될게요. 그리고 내 동생 민진이도 언니가 항상 사랑해~ 말은 항상 그렇게 해도 속으로는 항상 우리 동생 응원하고 있는 거 알지?

마지막으로, 우리 홈메 친구들 현빈, 수빈, 채은, 은서, 진아, 성민도 너무 고마워. 울산이라는 먼 곳에 오게 되어 6 년 이라는 시간이 흐르는 동안 너희들이 있었기 때문에 즐겁게 대학 생활을 보낼 수 있었어. 이제는 다들 흩어지고 있지만 그래두 종종 얼굴 보자!